

Forecasting and predicting stochastic agent-based model data with biologically-informed neural networks

John T. Nardini¹

¹*Department of Mathematics and Statistics, The College of New Jersey, Ewing, NJ, 08628, USA. ,
nardinij@tcnj.edu*

December 21, 2023

Abstract

Stochastic agent-based models (ABMs) are widely used to describe collective processes in ecology, epidemiology, and cellular biology. It is challenging to predict how ABMs behave over many parameter values due to their computational nature. Modelers often address this limitation by coarse-graining ABM rules into mean-field differential equation (DE) models. These DE models are advantageous because they are fast to simulate; unfortunately, DE models can provide poor ABM predictions (or be ill-posed) in certain regions of parameter space. In this work, we describe how biologically-informed neural networks (BINNs) can be trained to learn BINN-guided PDE models to predict ABM behavior. In particular, we show that BINN-guided PDE simulations can forecast future ABM data not seen during model training, and we can predict ABM data at previously-unexplored parameter values by combining BINN-guided PDE simulations with multivariate interpolation. We demonstrate our approach using three case study ABMs of collective migration. We find through these case studies that BINN-guided PDEs accurately forecast and predict ABM data with a one-compartment PDE when the mean-field PDE is ill-posed or requires two compartments. This work is broadly applicable to studying biological systems that exhibit collective behavior. All code and data from our study is available at https://github.com/johnnardini/Forecasting_predicting_ABMs.

1 Introduction

Many population-level patterns in biology arise from the actions of individuals. For example, predator-prey interactions determine ecological population dynamics; individuals' adherence to public health policies limit disease spread; and cellular interactions drive wound healing and tumor spread. Mathematical modeling is a useful tool to understand and predict how such individual actions scale into collective behavior [1, 2, 3, 4, 5, 6, 7]. In particular, stochastic agent-based models (ABMs) are a widely-used modeling framework

where autonomous agents mimic the individuals of a population [8, 9, 10, 11]. ABMs are advantageous because they capture the discrete and stochastic nature of many biological processes [12]. However, ABMs are computationally intensive, and their simulations can become time consuming when the population is comprised of many individuals [13, 14]. This computational restraint prevents modelers from efficiently exploring how model parameters alter model outputs. As such, there is a need for the development of methods to address ABMs' computational expenses by 1.) forecasting future model output from limited simulations, and 2.) predicting ABM data at previously-unexplored parameter values [14, 15, 16].

Modelers often perform ABM prediction by coarse-graining ABM rules into continuous differential equation (DE) models [8, 13]. Ordinary DEs (ODEs) describe how a single quantity (e.g., agent density) change over time, and Partial DEs (PDEs) describing how spatially-varying ABMs change with time [13]. Such DE models are useful surrogates for ABMs because they are cheap and efficient to simulate and are amenable to analytical methods, which modelers can use to precisely infer how model parameters impact their outputs. The most commonly used coarse-grained DE models are *mean-field DE models*, which are derived by assuming agents respond to the average behavior of their neighbors [14]. Mean-field DE models have been shown to accurately predict ABM behavior at certain model parameter values. Unfortunately, these models can poorly predict ABM outputs at other parameter values [8, 17]. For example, Baker and Simpson 2010 [8] demonstrated that the mean-field DE model for a population growth ABM only accurately predict ABM data when agents proliferate slowly. A further complication of mean-field DEs is that they may be ill-posed at certain parameter values. Anguige and Schmeiser 2009 [1] used a stochastic space-jump model to study how cell adhesion impacts collective migration and found that the resulting mean-field PDE model is ill-posed (and thus cannot predict ABM behavior) for large adhesion values. Modelers may improve DE models' predictive capability by implementing pair-wise interactions or moment closure approximations in lieu of the mean-field assumption, but the resulting models are often complicated and may significantly increase computation time [8, 18, 19].

Despite the inability of mean-field DE models to predict ABM behavior at some parameter values, all ABM simulations do obey conservation laws (e.g., conservation of mass for spatial ABMs) [20]. This observation suggests that alternative DE models may be capable of accurately describing ABM behavior. Equation learning (EQL) is a new area of research on the development and application of algorithms to discover the dynamical systems model that best describes a dataset [21, 22, 23, 24, 25, 26, 27, 28, 29, 30, 31]. Brunton et al. 2016 [21] introduced a sparse regression-based EQL approach to learn DE models from data with a user-specified library of candidate terms. This method has proven very successful in recovering informative models from simulated DE and PDE data as well as experimental data [32]. There is a growing understanding that EQL methods can aid the prediction of ABM data [14, 33, 34, 35]. For example, we recently demonstrated that the least squares EQL approach learns ODE equations that accurately describe simulated ABM data, even when the collected data is incomplete or sparsely sampled [14]. Supekar et al. 2023 [35] coupled this method with spectral basis representation data to discover PDE models that capture

the emergent behavior found in active matter ABMs. Another popular EQL approach includes physics-informed neural networks (PINNs), where modelers embed physical knowledge (in the form of a known PDE framework) into the training procedure for artificial neural networks (ANNs) [36, 37, 38, 39, 40]. Trained PINN models can predict complex, sparse, and noisy data while also obeying known physical principles. Lagergren et al. 2020 [30] extended the PINNs framework by replacing physics-based mechanistic terms with function-approximating multi-layer perceptions (MLPs) to develop the biologically-informed neural network (BINN) methodology. As a result, BINN models can learn PDE models from data with terms that depend on space, time, or agent density. Modelers can implement a PDE during BINN training that is similar to an ABM’s mean-field DE model; training the BINN to simulated ABM data ensures that a realization of this PDE that best matches the data is learned. BINNs thus present a promising tool for ABM forecasting and prediction, but determining how they can be used to learn predictive DE models remains an open area of research.

In this work, we demonstrate how to combine BINNs and PDE model simulations to forecast and predict ABM behavior. Our approach leverages BINNs’ vast data and modeling approximation capability with the computational efficiency of PDE models to develop a potent ABM surrogate modeling tool. In particular, we demonstrate how to use trained BINN models to forecast future ABM data at a fixed parameter, as well as how to predict ABM data at new parameter values by combining BINN modeling terms with multivariate interpolation. Interpolation provides a straightforward approach for inferring PDE modeling terms, though more complex methodologies, such as ANNs or Gaussian processes, could also be used [41].

This research fits into the research area of meta-modelling expensive computer simulation models, which is related to the design of computer experiments. Here, modelers implement computationally efficient statistical methods, or surrogate models, to emulate high-fidelity computer simulations [42, 43]. In a typical study, modelers calibrate the chosen surrogate model to several high fidelity computer simulations, and the calibrated surrogate model is utilized to perform a certain task, such as identifying sensitive model parameters, predicting new dynamics from the high fidelity simulation, or estimating its parameters from data. Modelers must choose a surrogate model to use: Gaussian processes are the most popular method thanks to the influential work of [41]. The Bayesian approximation error method is another widely-used technique [44, 45, 46], and ANNs have gained traction in recent years [16, 47]. While these ‘black-box’ model choices have proven successful in practice, they typically ignore domain expertise on the high-fidelity simulation, which limits the interpretability of their analyses. In this work, we implement a ‘gray-box’ approach for ABM prediction by training predictive BINN models to discover computationally efficient and interpretable surrogate PDE models [48]. Visual inspection of the PDE modeling terms enables us to interpret how model parameters impact ABM behavior at the population level. Our work is similar to [13], which built a statistical model to infer the discrepancy between ABM simulations and their coarse-grained ODE approximations; parameters with high discrepancies indicate the assumptions underlying model coarse-graining are invalid. In this previous study, incorporating the discrepancy model into the data’s statistical model allowed for

accurate ABM parameter estimation.

We apply the BINNs methodology to ABMs mimicking collectively migrating cell population in three separate case studies. Cellular migration plays an important role in embryo development, wound repair, and tumorigenesis [49, 50]. While migrating, cells experience and respond to various stimuli, including empty space, cell-cell interactions, chemical signals, chemical gradients, etc. There is thus a current need to establish the impacts of each of these stimuli on the collective migration of cell populations. Many models have been proposed to determine how each stimulus impact collective migration, including both continuous DEs and stochastic ABMs. However, continuous DE models may mispredict ABM behavior (or even be ill-posed for certain parameter values). Additionally, the continuous DE models may become quite complex when there are many ABM rules or types of agents that all interact with each other [6]. In each case study, we apply our BINNs methodology to learn nonlinear diffusion PDE models describing the spread of the collectively migrating population. The PDE framework for these models can be written as

$$\frac{\partial T}{\partial t} = \nabla \cdot (\mathcal{D}(T)\nabla T), \tag{1}$$

where $T = T(x, t)$ denotes the total spatiotemporal agent density and $\mathcal{D}(T)$ is the density-dependent agent diffusion rate. Each case study ABM consists of rules on the impacts of cell pulling and/or adhesion on collective migration. The first case study demonstrates that BINNs learn PDE models that closely match the mean-field PDE when the mean-field PDE accurately predicts ABM behavior. The second case study reveals that BINNs can learn predictive PDEs for ABMs, even when the corresponding mean-field PDE model is ill-posed. The third case study shows that BINNs can learn predictive and interpretable one-compartment PDEs when the mean-field PDE requires two compartments and is not interpretable due to its complexity. We implement our approach using Python (version 3.9.12), and all code is available on GitHub at https://github.com/johnnardini/Forecasting_predicting_ABMs.

We begin this work in Section 2 by presenting the case study ABMs and their mean-field PDE models. In Section 3, we discuss our data analysis methods on BINNs training and ABM forecasting and prediction. In Section 4, we detail our results on implementing these methods on the three case studies and finish this section with a brief discussion on the computational expenses of each data analysis method. We conclude these results and suggest areas for future work in Section 5.

2 Coarse-graining collectively migrating ABMs into PDE models

In this study, we apply our BINNs methodology to three case study ABMs, each of which models how cell-cell interactions (namely, cell pulling and adhesion) impact collective cell migration. Each of these ABMs are two-dimensional cellular automata with pulling agents that perform cell pulling rules and/or adhesive agents that perform rules on cell adhesion. The first model is borrowed from [12] and consists only of pulling agents; the second model is inspired by the stochastic space jump model from [1] and consists only of adhesive agents;

Parameter	Description	Range
r_m^{pull}	Pulling agent migration rate	$[0, \infty)$
r_m^{adh}	Adhesive agent migration rate	$[0, \infty)$
p_{pull}	Probability of successful pulling event	$[0, 1]$
p_{adh}	Probability of successful adhesion event	$[0, 1]$
α	Proportion of adhesive agents	$[0, 1]$

Table 1: Description of the ABM parameters involved in each ABM. The proportion of pulling agents in each simulation is given by $1 - \alpha$.

to the best of our knowledge, we are the first to study the third model, which consists of both pulling and adhesive agents.

In this section, we briefly introduce our case study ABMs and their rules on agent pulling and adhesion in Section 2.1; we detail our notation in Section 2.2; and we present the mean-field PDE models for each ABM in Section 2.3. More details on the ABM rules, implementation, and coarse-graining can be found in Appendices A, B, and D, respectively.

2.1 Brief introduction to the case study ABMs and their model rules

Rules A-F governing agent pulling and adhesion are visually depicted in Figure 1, and the parameters for each rule are described in Table 1. Our three case study ABMs are:

1. **The Pulling ABM**, which consists of rules A and B;
2. **The Adhesion ABM**, which consists of rules C and D;
3. **The Pulling & Adhesion ABM**, which consists of rules A-F.

In all rules, a *migrating agent* chooses one of its four neighboring lattice site to move into with equal probability (Figure 1(a)). A migration event is aborted if the lattice site in the chosen direction is already occupied (Figure 1(b)). We refer to a *neighboring agent* as an agent located next to the migrating agent in the direction opposite of the chosen migration direction.

Rules A, B, and E are initiated when a pulling agent attempts to migrate, which occurs with rate r_m^{pull} . Rules C, D, and F are initiated when an adhesive agent attempts to migrate, which occurs with rate r_m^{adh} . Each rule can be described as follows:

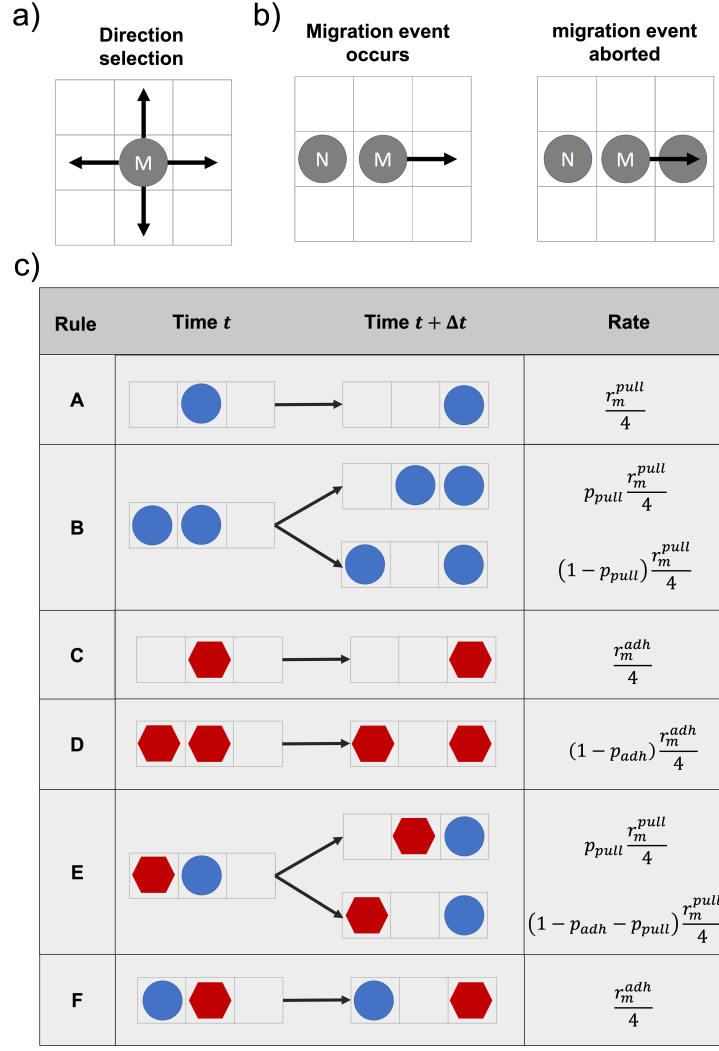


Figure 1: ABM rules on migration, pulling, and adhesion. a) When an agent performs a migration event, it chooses one of the four cardinal directions to move towards with equal probability. The migrating agent is referred to as a migrating agent (M) b) A migration event requires the lattice site in the chosen migration direction to be empty; otherwise, the migration event is aborted. A neighboring agent (N) is an agent located in the direction opposite the chosen migration direction. c) Rules A-F dictate the rules on agent migration, pulling, and adhesion. Here, we show each rule when an agent chooses to move rightwards. Rule A prescribes how a pulling agent (blue circle) migrates when there is no neighboring agent. Rule B prescribes how a pulling agent migrates and attempts to pull a neighboring pulling agent with it. Rule C prescribes how an adhesive agent (red hexagon) migrates when there is no neighboring agent. Rule D prescribes how a neighboring adhesive agent attempts to adhere to a migrating adhesive agent and abort its migration event. Rule E prescribes how a migrating pulling agent attempts to pull its neighboring adhesive agent, while the adhesive agent attempts to adhere to the pulling agent. Rule F prescribes how a migrating adhesive agent and neighboring pulling agent do not interact with each other. The last column documents the rate at which each lattice site configuration at time t changes to the updated lattice site configuration at time $t + \Delta t$.

Rule A occurs when a migratory pulling agent has no neighboring agent: the migrating pulling agent moves in the chosen direction.

Rule B occurs when a migratory pulling agent has a neighboring pulling agent:

- the migrating pulling agent pulls this neighboring pulling agent with probability p_{pull} , and both agents move in the chosen direction; or
- the pulling event fails with probability $1 - p_{adh}$, and only the migrating pulling agent moves in the chosen direction.

Rule C occurs when a migratory adhesive agent has no neighboring agent: the migrating adhesive agent moves in the chosen direction.

Rule D occurs when a migratory adhesive agent has a neighboring adhesive agent:

- the neighboring adhesive agent adheres to the migrating adhesive agent with probability p_{adh} , and the migration event is aborted; or
- the adhesion event fails with probability $1 - p_{adh}$, and the migrating agent moves in the chosen direction.

Rule E occurs when a migratory pulling agent has a neighboring adhesive agent:

- the migrating pulling agent pulls the neighboring adhesive agent with probability p_{pull} , and both agents move in the chosen direction;
- the neighboring adhesive agent adheres to the migrating pulling agent with probability p_{adh} , and the migration event is aborted; or
- the pulling and adhesion events both fail with probability $1 - p_{adh} - p_{pull}$, and the migrating pulling agent moves in the chosen direction.

Rule F occurs when a migratory adhesive agent has a neighboring pulling agent: the two agents do not interact, and the migrating adhesive agent freely moves in the chosen direction.

2.2 ABM Notation

Each model is simulated in the spatial domain $(x, y) \in [0, X] \times [0, Y]$. We choose $X = 200$ and $Y = 40$ to represent a thin rectangle where collective migration primarily occurs along the x -dimension and is not affected by the boundary in this dimension. We represent this space with a two-dimensional lattice with square lattice sites with length $\Delta = 1$ to imitate a typical cell length. Each model is an exclusion process, meaning that each agent can only occupy one lattice site at a time, and each lattice site is occupied by at most one agent. The variables $P_{i,j}(t)$, $H_{i,j}(t)$, and $0_{i,j}(t)$ denote the probabilities that lattice site (i, j) is occupied at time t by a pulling agent, adhesive agent, or empty, respectively for $i = 1, \dots, X$ and $j = 1, \dots, Y$.

Let $N_P^{(r)}(x_i, t)$ and $N_H^{(r)}(x_i, t)$ denote the number of pulling and adhesive agents, respectively, in the i^{th} column for $i = 1, \dots, X$ from the r^{th} of $R = 25$ identically prepared ABM simulations. To estimate the pulling and adhesive agent densities in the i^{th} column from the r^{th} simulation, we compute

$$P^{(r)}(x_i, t) = \frac{N_P^{(r)}(x_i, t)}{Y} \text{ and } H^{(r)}(x_i, t) = \frac{N_H^{(r)}(x_i, t)}{Y}, \quad i = 1, \dots, X,$$

respectively. The total agent density in the r^{th} simulation is then estimated by

$$T^{(r)}(x_i, t) = P^{(r)}(x_i, t) + H^{(r)}(x_i, t).$$

To estimate the averaged pulling, adhesive, and total agent density in the i^{th} column from R identically prepared ABM simulations over time, we compute:

$$\begin{aligned} \langle P^{ABM}(x_i, t) \rangle &= \frac{1}{R} \sum_{r=1}^R P^{(r)}(x_i, t); \\ \langle H^{ABM}(x_i, t) \rangle &= \frac{1}{R} \sum_{r=1}^R H^{(r)}(x_i, t); \text{ and} \\ \langle T^{ABM}(x_i, t) \rangle &= \frac{1}{R} \sum_{r=1}^R T^{(r)}(x_i, t), \text{ for } i = 1, \dots, X. \end{aligned}$$

2.3 The ABMs' mean-field PDE models

Here, we present the mean-field PDE models for each case study ABM.

2.3.1 The Pulling ABM

The Pulling ABM includes only pulling agents and thus consists of Rules A-B from Figure 1. In Appendix D.1, we show that these rules can be coarse grained into the Pulling ABM's mean-field PDE model:

$$\frac{\partial P}{\partial t} = \nabla \cdot (\mathcal{D}^{pull}(P) \nabla P), \quad \mathcal{D}^{pull}(P) = \frac{r_m^{pull}}{4} (1 + 3p_{pull} P^2) \quad (2)$$

where $P = P(x, y, t)$ denotes the spatiotemporal pulling agent density. In Figure 2(a-f), we find that a simulation of Equation (2) closely matches $P^{(1)}(x, t)$ over time for $\mathbf{p} = (r_m^{pull}, p_{pull})^T = (1.0, 0.5)^T$.

2.3.2 The Adhesion ABM

The Adhesion ABM includes only adhesive agents and thus consists of Rules C-D from Figure 1. In Appendix D.2, we show that these rules can be coarse grained into the Adhesion ABM's mean-field PDE model:

$$\frac{\partial H}{\partial t} = \nabla \cdot (\mathcal{D}^{adh}(H) \nabla H), \quad \mathcal{D}^{adh}(H) = \frac{3r_m^{adh}}{4} \left(p_{adh} \left(H - \frac{2}{3} \right)^2 + 1 - \frac{4p_{adh}}{3} \right) \quad (3)$$

where $H = H(x, y, t)$ denotes the spatiotemporal adhesive agent density. In Figure 2(g-l), we find that a simulation of Equation (3) closely matches $H^{(1)}(x, t)$ over time for $\mathbf{p} = (r_m^{adh}, p_{adh})^T = (1.0, 0.5)^T$.

It is important to note that $\mathcal{D}^{adh}(H)$ from Equation (3) becomes negative for some density values when $p_{adh} > 0.75$. This PDE thus fails to provide an ABM prediction at these parameter values because negative diffusion is ill-posed [1].

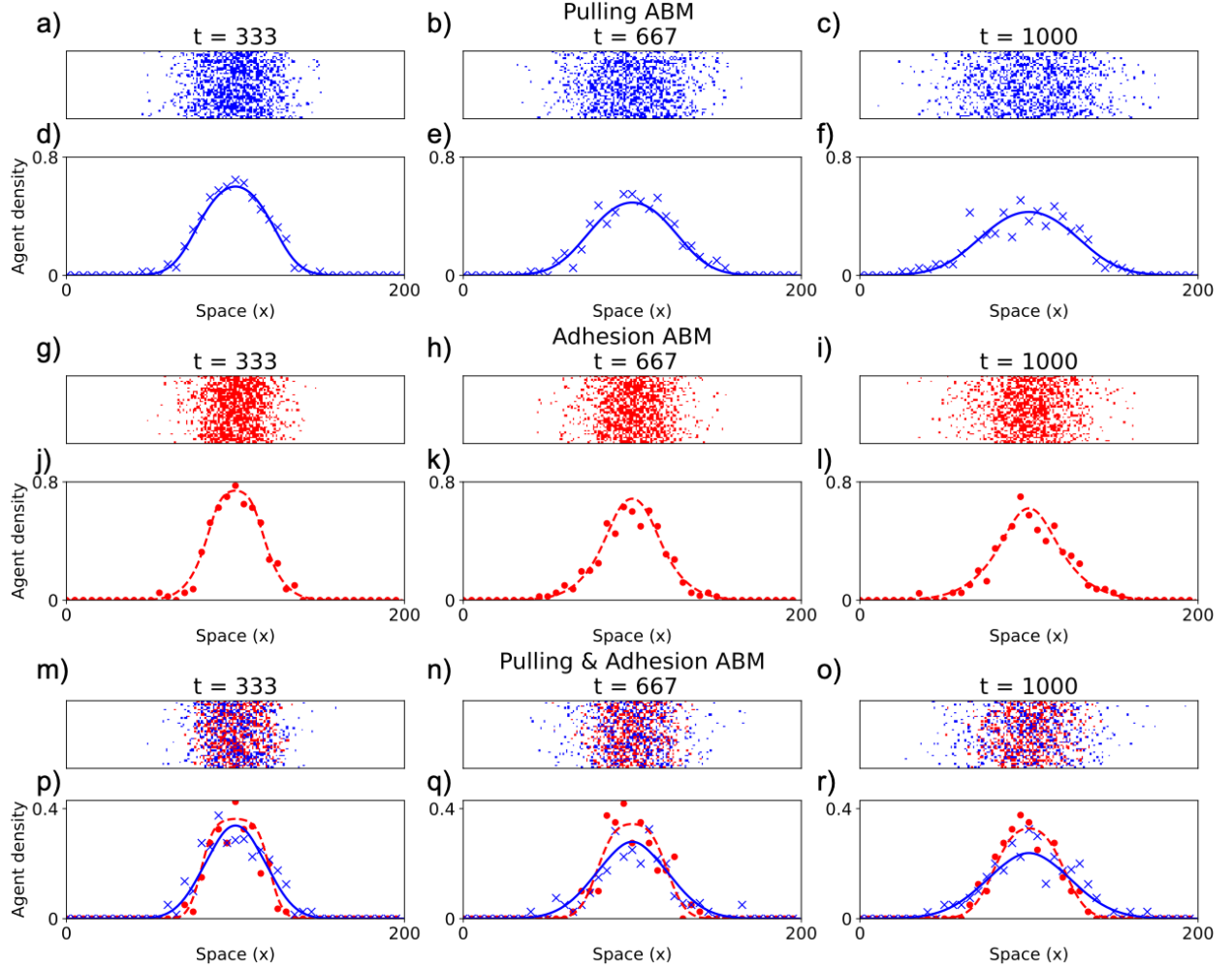


Figure 2: ABM simulation snapshots and the mean-field PDE models for the Pulling, Adhesion, and Pulling & Adhesion ABMs. Blue pixels denote pulling agents and red pixels denote adhesive agents. All ABMs were simulated on rectangular 200×40 lattices. (a-c) Snapshots of the Pulling ABM for $r_m^{pull} = 1.0, p_{pull} = 0.5$. (d-f) The output spatiotemporal pulling agent density (blue 'x' marks) is plotted against the solution of the mean-field PDE (solid blue line) given by Equation (2). (g-i) Snapshots of the Adhesion ABM for $r_m^{adh} = 1.0, p_{adh} = 0.5$. (j-l) The output spatiotemporal adhesive agent density (red dots) is plotted against the solution of the mean-field PDE (dashed red line) given by Equation (3). (m-o) Snapshots of the Pulling & Adhesion ABM for $r_m^{pull} = 1.0, r_m^{adh} = 0.25, p_{pull} = 0.033, p_{adh} = 0.33, \alpha = 0.5$. (p-r) The output spatiotemporal pulling and adhesive agent densities are plotted against the solution of the mean-field PDE given by Equation (4).

2.3.3 The Pulling & Adhesion ABM

The Pulling & Adhesion ABM includes both pulling and adhesive agents, and thus consists of Rules A-F from Figure 1. In Appendix D.3, we show that these rules can be coarse-grained into the Pulling & Adhesion ABM’s mean-field PDE model:

$$\begin{aligned}
\frac{\partial P}{\partial t} &= \frac{r_m^{pull}}{4} \nabla \cdot \left((1-T) \nabla P + P \nabla T \right) \\
&\quad + p_{adh} \frac{r_m^{pull}}{4} \nabla \cdot \left(-3P(1-T) \nabla H - H(1-T) \nabla P - HP \nabla T \right) \\
&\quad + p_{pull} \frac{r_m^{pull}}{4} \nabla \cdot \left(3P^2 \nabla T \right) \\
\frac{\partial H}{\partial t} &= \frac{r_m^{adh}}{4} \nabla \cdot \left((1-T) \nabla H + H \nabla T \right) \\
&\quad + p_{adh} \frac{r_m^{adh}}{4} \nabla \cdot \left(-4(1-T)H \nabla H - H^2 \nabla T \right) \\
&\quad + p_{pull} \frac{r_m^{pull}}{4} \nabla \cdot \left(-(1-T)H \nabla P + (1-T)P \nabla H + 3HP \nabla T \right). \tag{4}
\end{aligned}$$

This two-compartment PDE describes the spatiotemporal densities of pulling agents, $P(x, y, t)$, and adhesive agents, $H = H(x, y, t)$. The *total agent density* is given by $T = T(x, y, t) = H(x, y, t) + P(x, y, t)$. In Figure 2(m-r), we find that the P and H compartments from a simulation of Equation (4) closely $P^{(1)}(x, t)$ and $H^{(1)}(x, t)$, respectively, over time for $\mathbf{p} = (r_m^{pull}, r_m^{adh}, p_{pull}, p_{adh}, \alpha)^T = (1.0, 0.25, 0.33, 0.33, 0.5)^T$. To the best of our knowledge, it is not possible to convert Rules A-F into a single-compartment PDE model describing $T(x, y, t)$

3 Data analysis methods

Our data analysis pipeline is visually depicted in Figure 3. We first simulate all three case study ABMs over a range of agent migration, pulling, and adhesion parameter values; we represent model parameters with the vector \mathbf{p} . Each model simulation outputs 100 snapshots of agent configurations over time; from each simulation, we generate the one-dimensional agent density along the x -dimension over time. We average these densities over $R = 25$ simulations to obtain the final output ABM density, $\langle T^{ABM}(x, t; \mathbf{p}) \rangle$. We use the data from the first 75 timepoints as training data and the final 25 timepoints as testing data. BINN models consist of a data-approximating MLP, $T^{MLP}(x, t)$, and a diffusion rate-approximating MLP, $\mathcal{D}^{MLP}(T)$. We train T^{MLP} to closely approximate the ABM training data while T^{MLP} and \mathcal{D}^{MLP} satisfy Equation (1). After BINN training, the inferred $\mathcal{D}^{MLP}(T)$ function is used to forecast and predict ABM data. To forecast ABM training and testing data, we simulate Equation (1) in one spatial dimension with $\mathcal{D} = \mathcal{D}^{MLP}(T)$. To predict ABM data at a new parameter value, \mathbf{p}^{new} , we perform interpolation over several previously-inferred diffusion rate MLPs, $\mathcal{D}^{MLP}(T; \mathbf{p}_i)$ for $i = 1, \dots, K_1$, and then simulate the diffusion PDE framework using the resulting interpolant, $\mathcal{D}^{interp}(T; \mathbf{p}^{new})$. The python files and notebook used for all steps of our analysis

are presented in https://github.com/johnnardini/Forecasting_predicting_ABMs.

3.1 Simulating ABM data

We simulate ABM data by simulating each model over many parameter values, \mathbf{p} (Part 1 from Figure 3). For each \mathbf{p} , we simulate $R = 25$ identically prepared realizations of the ABM; each realization is completed when time reaches $t = 1000$. We estimate the total spatiotemporal agent density from each simulation and average over all R simulations to obtain $\langle T^{ABM}(x, t) \rangle = \{\langle T^{ABM}(x_i, t_j) \rangle\}_{i=1, \dots, X}^{j=1, \dots, 100}$, where $x_i = i\Delta x$ and $t_j = (j - 1)\Delta t$ for $\Delta x = 1$ and $\Delta t = 10$. We split $\langle T^{ABM}(x, t) \rangle$ into its training and testing datasets by setting $\langle T^{ABM}(x, t) \rangle^{train} = \{\langle T^{ABM}(x_i, t_j) \rangle\}_{i=1, \dots, X}^{j=1, \dots, T_f^{train}}$ and $\langle T^{ABM}(x, t) \rangle^{test} = \{\langle T^{ABM}(x_i, t_j) \rangle\}_{i=1, \dots, X}^{j=T_f^{train}+1, \dots, T_f^{test}}$. We set $T_f^{train} = 75$ and $T_f^{test} = 100$ to place 75% of data into the training dataset.

3.2 Training Biologically-informed Neural Networks (BINNs) to ABM data

We construct BINN models that consist of two sequential multilayer perceptron (MLP) models: $T^{MLP}(x, t)$ predicts the total agent density at the point (x, t) , and $\mathcal{D}^{MLP}(T)$ predicts the agent diffusion rate at the density value T (Part 2 of Figure 3). We train these two MLPs so that $T^{MLP}(x, t) \approx \langle T^{ABM}(x, t) \rangle^{train}$ while the two MLPs also satisfy Equation (1) in one spatial dimension:

$$\frac{\partial}{\partial t} T^{MLP} = \frac{\partial}{\partial x} \left(\mathcal{D}^{MLP}(T^{MLP}) \frac{\partial}{\partial x} T^{MLP} \right). \quad (5)$$

We chose this nonlinear diffusion PDE framework for BINN model training because the mean-field models for the Pulling ABM and Adhesion ABM from Section 2 obey this framework with different diffusion rates.

More information on our implementation and training procedure for BINNs is provided in Appendix E; in particular, we detail the BINNs model architecture in Appendix E.1, the loss function in Appendix E.2, and our training procedure in Appendix E.3.

3.3 Forecasting ABM data

We use mean-field PDEs and BINN-guided PDEs to forecast ABM data (Part 3a of Figure 3). Most¹ of these PDEs are one-compartment nonlinear diffusion equations that can be written in one spatial dimension as

$$\frac{\partial T}{\partial t} = \frac{\partial}{\partial x} \left(\mathcal{D}(T) \frac{\partial T}{\partial x} \right), \quad (6)$$

where $T = T(x, t)$ is the total agent density and $\mathcal{D}(T)$ is a density-dependent rate of diffusion. Recall that for the Pulling ABM, $T(x, t) = P(x, t)$; for the Adhesion ABM, $T(x, t) = H(x, t)$; and for the Pulling & Adhesion ABM, $T(x, t) = P(x, t) + H(x, t)$.

¹The mean-field PDE for the Pulling & Adhesion ABM is instead given by the two-compartment PDE from Equation (4).

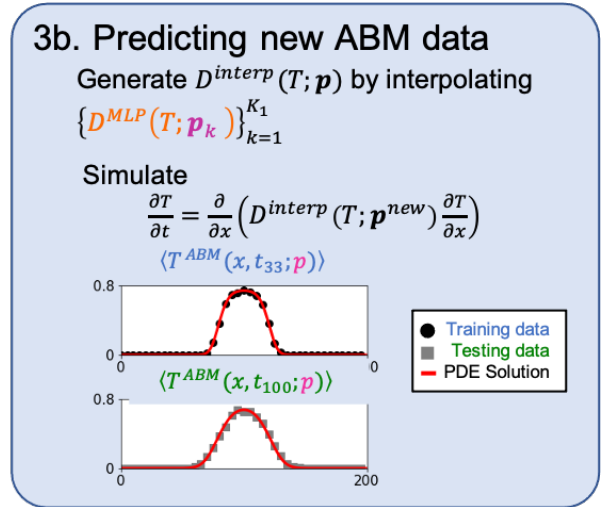
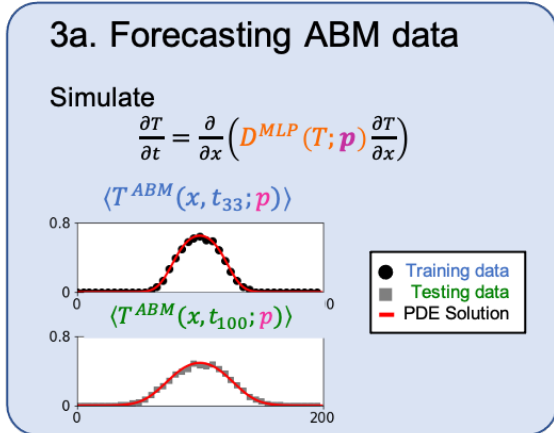
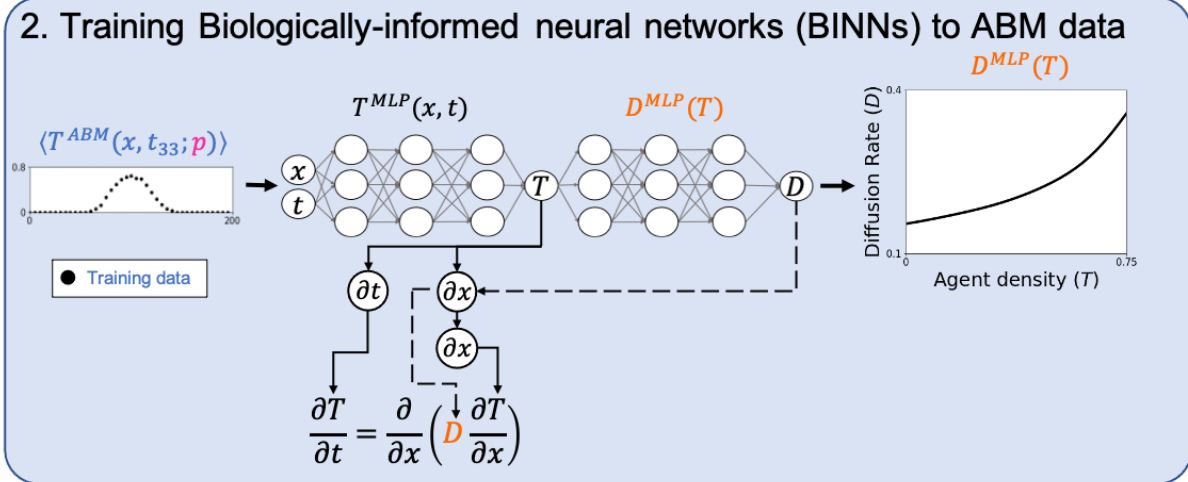
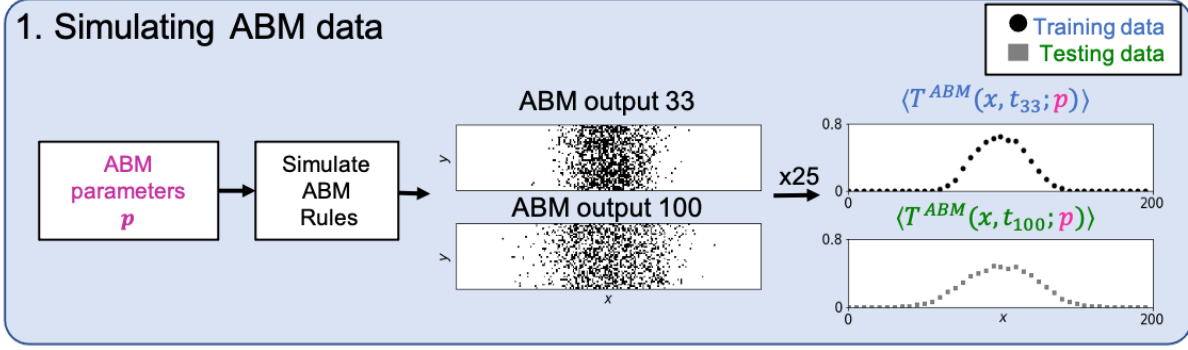


Figure 3: Data analysis pipeline. 1. Simulating ABM data For a given parameter, p , we simulate the Pulling, Adhesion, or Pulling & Adhesion ABM. Each model outputs snapshots of pulling and adhesive agent locations over time; we summarize this data by estimating the average total agent density along the x -direction for each snapshot (not shown). We perform 25 total ABM simulations for each p and average the total spatiotemporal agent density to obtain $\langle T^{ABM}(x, t; p) \rangle$. The first 75 timepoints are placed into a training ABM dataset, and the final 25 timepoints are placed into a testing ABM dataset. 2. Training biologically-informed neural networks (BINNs) to ABM data. Each BINN model consists of a data-approximating MLP, $T^{MLP}(x, t)$, and a diffusion-rate-approximating MLP, $D^{MLP}(T)$. BINN models are trained so that $T^{MLP}(x, t) \approx \langle T^{ABM}(x, t) \rangle^{train}$ while T^{MLP} and D^{MLP} satisfy Equation (1). After model training, the inferred $D^{MLP}(T)$ estimates the agent diffusion rate. 3a. Forecasting ABM data. Simulating the diffusion PDE framework with D^{MLP} allows us to forecast the ABM training and testing data. 3b. Predicting new ABM data. We predict the rate of agent diffusion at a new parameter, p^{new} , by interpolating $D^{MLP}(T; p)$ over several p values to create D^{interp} . Simulating the diffusion PDE framework with D^{interp} allows us to predict the new ABM training and testing data.

For the mean-field PDE models, we simulate Equation (6) with $\mathcal{D}(P) = \mathcal{D}^{pull}(P)$ from Equation (2) for the Pulling ABM, and $\mathcal{D}(H) = \mathcal{D}^{adh}(H)$ from Equation (3) for the Adhesion ABM. The mean-field PDE for the Pulling & Adhesion ABM is given by the two-compartment PDE in Equation (4). For BINN-guided PDE models, we train a BINN model to $\langle T^{ABM}(x, t) \rangle^{train}$ (see Section 3.2) and then simulate Equation (6) where $\mathcal{D}(T)$ is the $\mathcal{D}^{MLP}(T)$ that results from BINN model training. Our implementation method to numerically integrate Equation (6) is provided in Appendix F.

We partition each PDE simulation, $T(x, t) = \{T(x_i, t_j)\}_{i=1, \dots, X}^{j=1, \dots, 100}$, into training and testing datasets to match the training and testing ABM datasets:

$$T(x, t)^{train} = \{T(x_i, t_j)\}_{i=1, \dots, X}^{j=1, \dots, T_f^{train}}, \quad T(x, t)^{test} = \{T(x_i, t_j)\}_{i=1, \dots, X}^{j=T_f^{train}+1, \dots, T_f^{train}}.$$

We report the training mean-squared error (MSE) from each simulation as:

$$\frac{1}{X T_f^{train}} \sum_{i=1, j=1}^{X, T_f^{train}} (T(x_i, t_j) - \langle T^{ABM}(x_i, t_j) \rangle)^2,$$

and the testing MSE as:

$$\frac{1}{X(T_f^{test} - T_f^{train})} \sum_{i=1, j=T_f^{train}+1}^{X, T_f^{test}} (T(x_i, t_j) - \langle T^{ABM}(x_i, t_j) \rangle)^2.$$

3.4 Predicting new ABM data

We use multivariate interpolation on previously-computed BINN-guided diffusion rates to predict density-dependent diffusion rates for new ABM data (Part 3b of Figure 3). We define a prior parameter collection and a new parameter collection as

$$\mathcal{P}^{prior} = \{\mathbf{p}_k\}_{k=1}^{K_1} \text{ and } \mathcal{P}^{new} = \{\mathbf{p}_k^{new}\}_{k=1}^{K_2}.$$

Our workflow for predicting ABM data from \mathcal{P}^{new} proceeds as follows:

1. Generate the prior and new ABM data collections by simulating the ABM at all parameters from the prior and new parameter collections:

$$\mathcal{T}^{prior} = \left\{ \langle T^{ABM}(x, t; \mathbf{p}_k) \rangle \right\}_{k=1}^{K_1} \text{ and } \mathcal{T}^{new} = \left\{ \langle T^{ABM}(x, t; \mathbf{p}_k^{new}) \rangle \right\}_{k=1}^{K_2}.$$

2. Train a BINN model to each training ABM dataset from \mathcal{T}^{prior} and extract $\mathcal{D}^{MLP}(T; \mathbf{p}_k)$ from the trained BINN model.
3. Perform multivariate interpolation on $\{\mathcal{D}^{MLP}(T; \mathbf{p}_k)\}_{k=1}^{K_1}$ to create an interpolant, $\mathcal{D}^{interp}(T; \mathbf{p})$, that matches the concatenated vector $[T, \mathbf{p}_k]$ to the diffusion rate $\mathcal{D}^{MLP}(T; \mathbf{p}_k)$ for $k = 1, \dots, K_1$.
4. Predict the new ABM dataset, $\langle T^{ABM}(x, t; \mathbf{p}_k^{new}) \rangle$, by simulating Equation (6) with $\mathcal{D} = \mathcal{D}^{interp}(T; \mathbf{p}_k^{new})$ to create $T^{interp}(x, t; \mathbf{p}_k^{new})$. Partition $T^{interp}(x, t; \mathbf{p}_k^{new})$ into its training and testing datasets to match the ABM data's training and testing datasets.

Model	Training MSE	Testing MSE
Artificial neural network	1.17×10^{-4}	9.36×10^{-4}
Biologically-informed neural network	9.32×10^{-5}	1.47×10^{-4}
Mean-field PDE	7.45×10^{-5}	1.00×10^{-4}
BINN-guided PDE	7.64×10^{-5}	1.02×10^{-4}

Table 2: Computed MSE values when forecasting $\langle T^{ABM}(x, t) \rangle^{train}$ and $\langle T^{ABM}(x, t) \rangle^{train}$ from the Pulling ABM with $\mathbf{p} = (r_m^{pull}, p_{pull})^T = (1.0, 0.5)^T$ using an ANN, BINN, mean-field PDE, or BINN-guided PDE.

5. Compute the training and testing MSEs between $T^{interp}(x, t; \mathbf{p}_k^{new})$ and $\langle T^{ABM}(x, t) \rangle$ to summarize the predictive performance of $T^{interp}(x, t; \mathbf{p}_k^{new})$ for $k = 1, \dots, K_2$.

We implement multi-dimensional radial basis function interpolation using Sci-kit Learn’s (version 0.24.2) **RBFInterpolator** command to create $\mathcal{D}^{interp}(T; \mathbf{p})$.

4 Results

4.1 PDE simulations outperform neural networks in ABM forecasting

We investigate the performance of an ANN, BINN, BINN-guided PDE model, and mean-field PDE model in forecasting ABM data. We simulated the Pulling ABM with $\mathbf{p} = (r_m^{pull}, p_{pull})^T = (1.0, 0.5)^T$ to generate the ABM data. The ANN was trained to minimize the loss function \mathcal{L}_{WLS} from Supplementary Equation (27), whereas the BINN was trained to minimize \mathcal{L}_{total} from Supplementary Equation (26). Both PDE models simulate Equation (6): for the BINN-guided PDE, $\mathcal{D} = \mathcal{D}^{MLP}$ from the trained BINN model; for the mean-field PDE, $\mathcal{D} = \mathcal{D}^{pull}$ from Equation (2).

Visual inspection suggests that all four models match the ABM training data well (Figure 4(a-b)²), though the computed training MSE values reveal that the mean-field and BINN-guided PDEs outperform the neural networks in describing this data (Table 2). The BINN, BINN-guided PDE, and mean-field PDE all accurately forecast the testing data (Figure 4(c)), but the two PDE models achieve smaller MSE values than the BINN model (Table 2). The ANN’s prediction for the testing data has a protrusion that overpredicts all data for $x > 125$ (Figure 4(c) inset), which causes this model’s computed testing MSE value to be almost an order of magnitude higher than all others.

4.2 Forecasting ABM data with BINN-guided and mean-field PDE simulations

We investigate the performance of BINN-guided and mean-field PDE simulations in forecasting the training and testing ABM datasets from the Pulling, Adhesion, and Pulling & Adhesion ABMs. See Section 3.3 for implementation details.

²the mean-field PDE is not plotted in this figure because it is visually indistinguishable from the BINN-guided PDE.

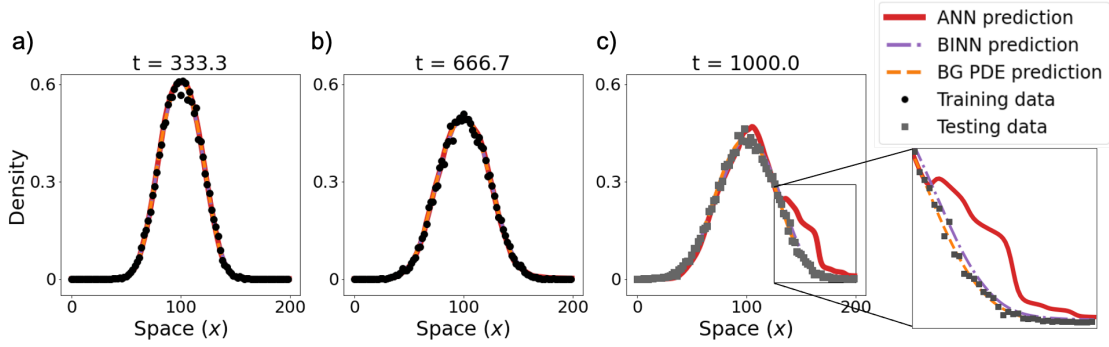


Figure 4: Forecasting ABM data with neural networks and PDEs. ANN and BINN models were trained to fit $\langle T^{ABM}(x, t) \rangle^{train}$ from the Pulling ABM with $\mathbf{p} = (r_m^{pull}, p_{pull})^T = (1.0, 0.5)^T$. These two ANNs and the mean-field and BINN-guided (BG) PDE simulations were then used to forecast (a-b) $\langle T^{ABM}(x, t) \rangle^{train}$ and (c) $\langle T^{ABM}(x, t) \rangle^{test}$. The mean-field PDE simulation is not plotted here because it is visually indistinguishable from the BG PDE simulation.

4.2.1 The BINN-guided and mean-field PDEs both accurately forecast Pulling ABM data

The parameters for the Pulling ABM are $\mathbf{p} = (r_m^{pull}, p_{pull})^T$. To evaluate the BINN-guided and mean-field PDE models' performances in forecasting Pulling ABM data over a range of agent pulling parameter values, we computed eleven ABM datasets by varying $p_{pull} = 0.0, 0.1, 0.2, \dots, 1.0$ while fixing $r_m^{pull} = 1.0$. The inferred rates of agent diffusion from both models propose that agents diffuse slower for low densities and faster for high densities, and that larger values of p_{pull} lead to increased density-dependent diffusion rates (Figure 5(a)). The two PDE models achieve comparable training and testing MSE values for all values of p_{pull} , though the mean-field PDE usually attains slightly smaller values (Figure 5(b)). Snapshots of both simulated PDE models against data shows that their ABM predictions are visually indistinguishable (Supplementary Figure 12(a-c)).

To evaluate both PDE models' performances over a range of pulling agent migration values, we computed ten Pulling ABM datasets with $r_m^{pull} = 0.1, 0.2, \dots, 1.0$ while fixing $p_{pull} = 0.5$. We find close agreement between both models' inferred diffusion rates for values of r_m^{pull} (Figure 5(c)). As a result, both models achieve similar computed training and testing MSE values (Figure 5(d)). Snapshots of both simulated PDE models against data reveals that their ABM predictions are visually indistinguishable (Supplementary Figure 12(d-f)).

4.2.2 BINN-guided PDEs accurately forecast Adhesion ABM data when the mean-field PDE is ill-posed

The parameters for the pulling ABM are $\mathbf{p} = (r_m^{adh}, p_{adh})^T$. To evaluate the BINN-guided and mean-field PDE models' performances over a range of agent adhesion parameter values, we computed eleven ABM

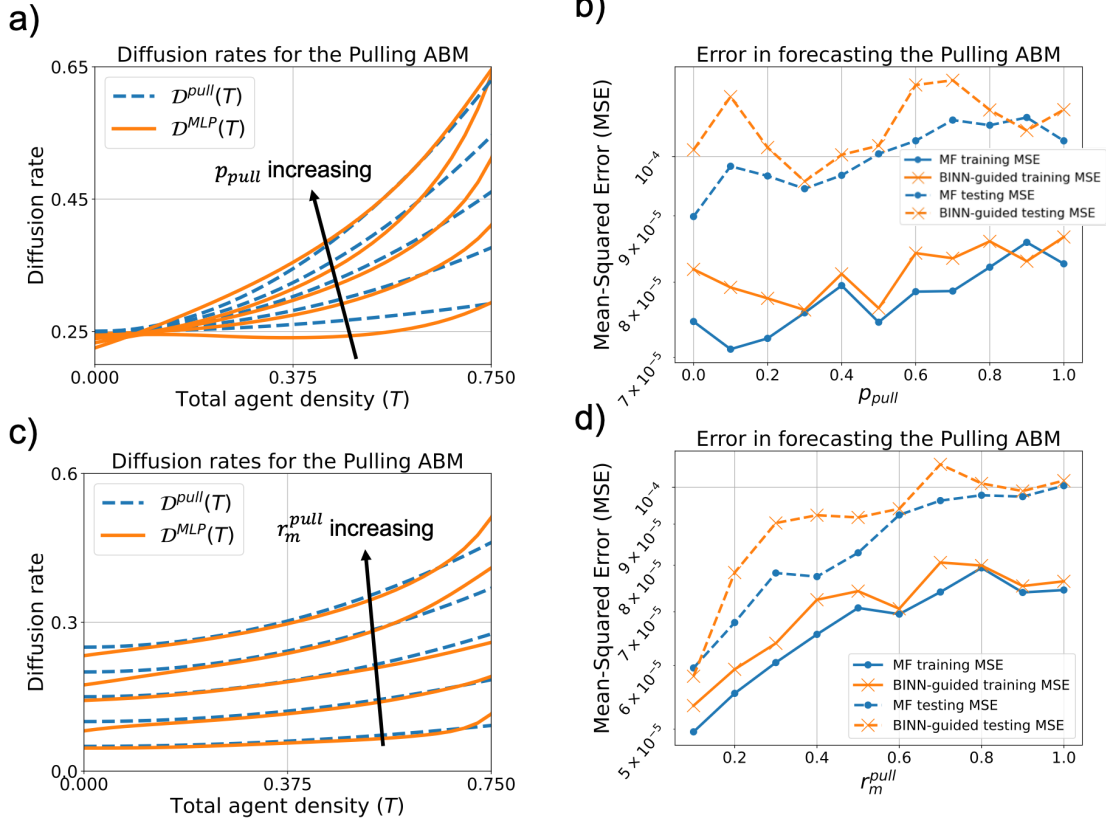


Figure 5: Forecasting Pulling ABM data with the mean-field (MF) and BINN-guided PDEs. (a) Plots of the mean-field diffusion rate, $\mathcal{D}^{pull}(T)$, from Equation (2) and the inferred BINN diffusion rate, $\mathcal{D}^{MLP}(T)$, for $p_{pull} = 0.1, 0.3, \dots, 0.9$ (results not shown for $p_{pull} = 0.0, 0.2, \dots, 1.0$ for visual ease) while fixing $r_m^{pull} = 1.0$. (b) Plots of the mean-field and BINN-guided PDEs' computed training and testing MSE values while varying p_{pull} and fixing $r_m^{pull} = 1.0$. (c) Plots of $\mathcal{D}^{pull}(T)$ and $\mathcal{D}^{MLP}(T)$ for $r_m^{pull} = 0.2, 0.4, \dots, 1.0$ while fixing $p_{pull} = 0.5$. (d) Plots of the mean-field and BINN-guided PDEs' computed training and testing MSE values while varying r_m^{pull} and fixing $p_{pull} = 0.5$.

datasets by varying $p_{adh} = 0.0, 0.1, 0.2, \dots, 1.0$ while fixing $r_m^{adh} = 1.0$. The inferred rates of agent diffusion from both models decrease with agent density for most values of p_{adh} (Figure 6(a)). When $p_{adh} = 0$, BINN-guided diffusion rate is slightly increasing and the mean-field model’s diffusion rate is constant. The BINN-guided diffusion rates decline faster with agent density than the corresponding mean-field diffusion rates for low density values. Both models agree that the density-dependent rates of diffusion fall as p_{adh} increases. We computed the training and testing MSEs for both models for all values of p_{adh} (Figure 6(b)) and partition the results as follows :

- **When $p_{adh} < 0.5$:** both models achieve similar training MSE values near 7×10^{-5} and testing MSE values around 10^{-4} .
- **When $0.5 \leq p_{adh} \leq 0.75$:** the mean-field PDE models’ training and testing MSE values increase as p_{adh} increases, with a maximum computed value above 3×10^{-4} . The BINN-guided PDE model’s training and testing MSE values remain near 7×10^{-5} and 10^{-4} , respectively.
- **When $p_{adh} > 0.75$:** the mean-field PDE model is ill-posed and cannot forecast this ABM data. The BINN-guided PDE model’s computed training and testing MSE values increase as p_{adh} increases, with a maximum computed value of 2×10^{-4} .

Close inspection of snapshots from both PDE model simulations against ABM data from $p_{adh} = 0.7$ reveals that the mean-field PDE model slightly overpredicts the data at high densities above 0.5 and low densities below 0.1, whereas the BINN-guided PDE closely matches the data (Supplementary Figure 13(c) inset).

To evaluate both PDE models’ performances over a range of adhesive agent migration values, we computed ten ABM datasets with $r_m^{adh} = 0.1, 0.2, \dots, 1.0$ while fixing $p_{adh} = 0.5$. Both PDE models similarly propose that agent density-dependent diffusion rates decrease for larger agent density values and that these rates increase for larger values of r_m^{adh} (Figure 6(c)). Both PDEs achieve similar computed training and testing MSE values for most values of r_m^{adh} (Figure 6(d)). When $r_m^{adh} = 0.1$, however, the BINN-guided PDE’s testing MSE value is close to 10^{-4} , whereas the mean-field PDE attains a lower testing MSE value near 6×10^{-5} . Despite these differences, the two model simulations appear similar at these parameter values (Supplementary Figure 13(d-f)).

4.2.3 BINN-guided PDEs accurately forecast Pulling & Adhesion ABM data with a one-compartment model

The parameters for the Pulling & Adhesion ABM are $\mathbf{p} = (r_m^{pull}, r_m^{adh}, p_{pull}, p_{adh}, \alpha)^T$. We evaluate the performance of the BINN-guided and mean-field DE models in forecasting data from the Pulling & Adhesion ABM. We created 48 ABM datasets by fixing the base parameter values at $\mathbf{p}_{base} = (1.0, 0.25, 0.33, 0.33, 0.5)^T$ and then varying one parameter at a time over several values. We vary $r_m^{pull} = 0.5, 0.6, \dots, 1.5$; $r_m^{adh} = 0.0, 0.1, \dots, 1.0$; $p_{pull} = 0.1, 0.2, \dots, 0.6, 0.67$; $p_{adh} = 0.1, 0.2, \dots, 0.6, 0.67$; and $\alpha = 0.0, 0.1, \dots, 1.0$. These parameter values were chosen to always satisfy $p_{pull} + p_{adh} \leq 1$.

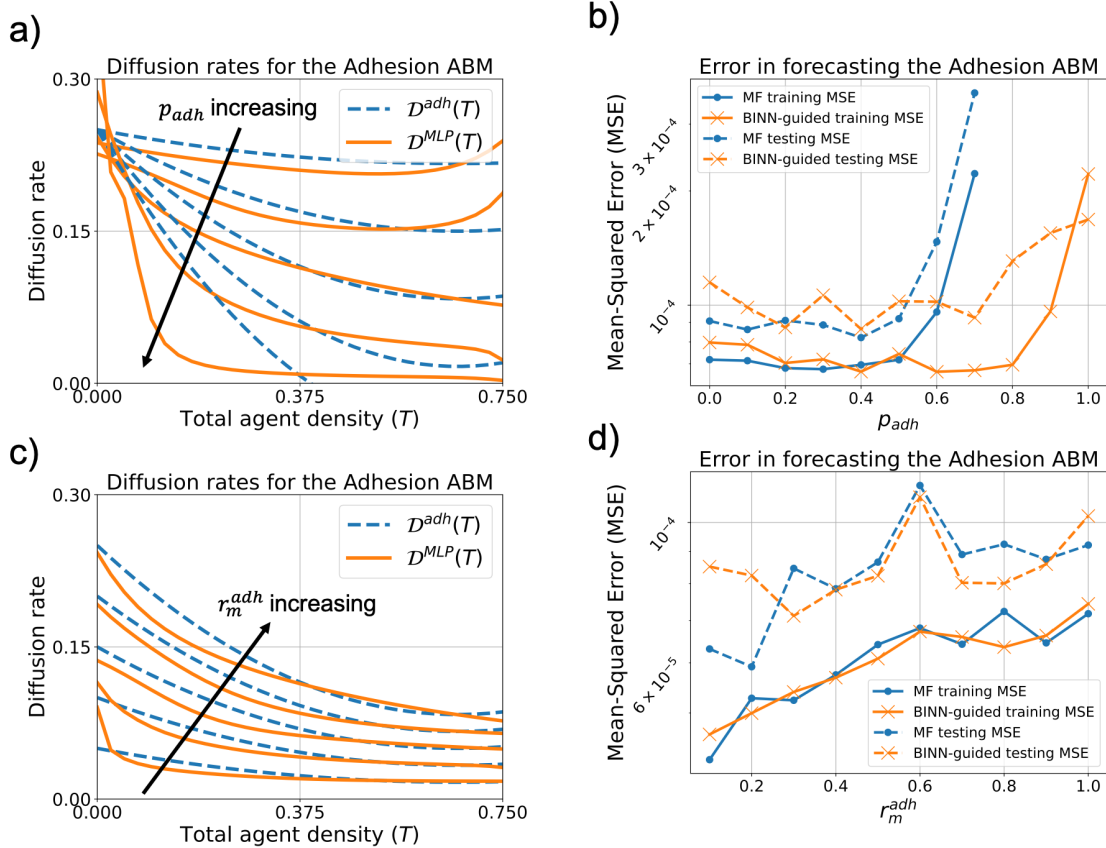


Figure 6: Forecasting Adhesion ABM data with the mean-field (MF) and BINN-guided PDEs. (a) Plots of the mean-field diffusion rate, $\mathcal{D}^{adh}(T)$, from Equation (3) and the inferred BINN diffusion rate, $\mathcal{D}^{MLP}(T)$, for $p_{adh} = 0.1, 0.3, \dots, 0.9$ (results not shown for $p_{adh} = 0.0, 0.2, \dots, 1.0$ for visual ease) while fixing $r_m^{adh} = 1.0$. (b) Plots of the mean-field and BINN-guided PDEs' computed training and testing MSE values while varying p_{adh} and fixing $r_m^{adh} = 1.0$. (c) Plots of $\mathcal{D}^{adh}(T)$ and $\mathcal{D}^{MLP}(T)$ for $r_m^{adh} = 0.2, 0.4, \dots, 1.0$ while fixing $p_{adh} = 0.5$. (d) Plots of the mean-field and BINN-guided PDEs' computed training and testing MSE values while varying r_m^{adh} and fixing $p_{adh} = 0.5$.

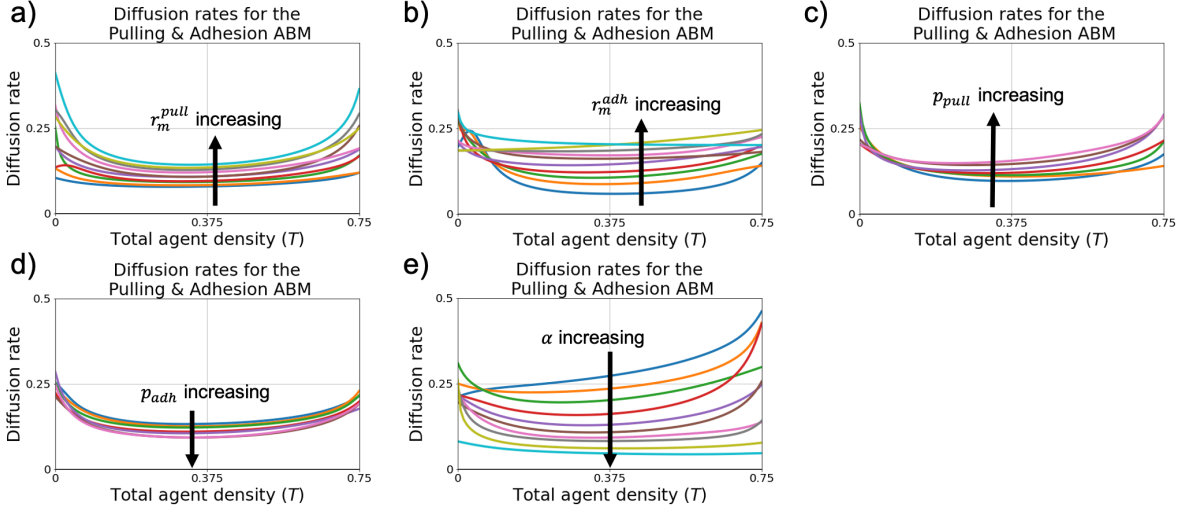


Figure 7: The inferred BINN diffusion rates for Pulling & Adhesion ABM data. Plots of the inferred BINN diffusion rate, $\mathcal{D}^{MLP}(T)$, when varying (a) r_m^{pull} , (b) r_m^{adh} , (c) p_{pull} , (d) p_{adh} , (e) α .

The BINN models' inferred diffusion rates, $\mathcal{D}^{MLP}(T; \mathbf{p})$, are often U-shaped with larger diffusion values at low and high agent densities and smaller values at intermediate densities (Figure 7). This U-shape tends to increase for larger values of r_m^{pull} , r_m^{adh} , and p_{pull} and decrease for larger values of p_{adh} and α . The inferred diffusion rates appear most sensitive to changes in the α parameter: at $\alpha = 0.0$, $\mathcal{D}^{MLP}(T; \mathbf{p})$ strictly increases with agent density and attains an average value of 0.289; at $\alpha = 1.0$, $\mathcal{D}^{MLP}(T; \mathbf{p})$ is strictly decreasing and has an average value of 0.051. The inferred diffusion rate is also sensitive to the r_m^{adh} and r_m^{pull} parameters: varying r_m^{adh} primarily alters the BINN diffusion rate at intermediate agent density values, whereas varying r_m^{pull} changes the BINN diffusion rate at low and high agent density values.

Recall that the BINN-guided PDE computes a single compartment to forecast the total agent density, $T(x, t)$, whereas the mean-field PDE computes two compartments forecasting the Pulling and Adhesive agent densities, $P(x, t)$ and $H(x, t)$, respectively. We forecast the total agent density with the mean-field PDE by setting $T(x, t) = P(x, t) + H(x, t)$. The BINN-guided and mean-field PDE models achieve similar training MSE values for most parameter values that we considered (Figure 8). The mean-field model's testing MSE values are often smaller than the BINN-guided testing MSE values, though the BINN-guided PDE also achieves small testing MSE values. For example, both PDE simulations accurately predict ABM data when p_{adh} is set to 0.4, but visualizing both PDE simulations shows that the mean-field PDE better matches the elbow of the data than the BINN-guided PDE (Supplementary Figure 14(a-c)). The BINN-guided PDE outperforms the mean-field PDE in forecasting data for small values of r_m^{adh} : plotting both PDE simulations against data from $r_m^{adh} = 0.1$ shows that the mean-field PDE underpredicts the largest agent density values, while the BINN-guided PDE accurately matches this data (Supplementary Figure 14(d-f)).

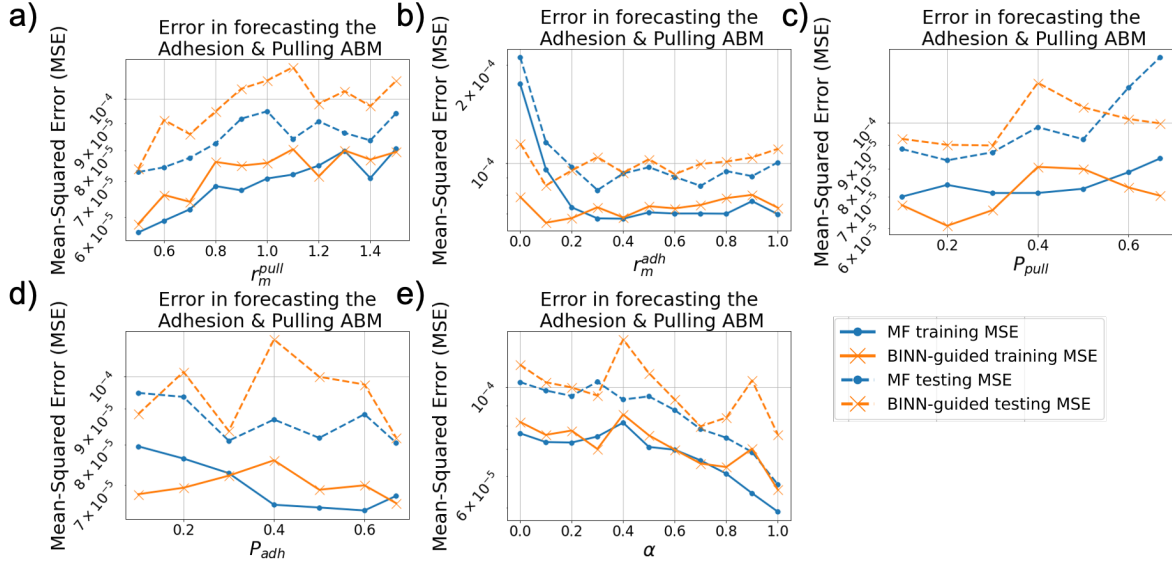


Figure 8: Forecasting Pulling & Adhesion ABM data with the mean-field and BINN-guided PDEs. Plots of the mean-field and BINN-guided PDEs’ computed training and testing values while varying (a) r_m^{pull} , (b) r_m^{adh} , (c) p_{pull} , (d) p_{adh} , (e) α .

4.3 Predicting ABM data at new parameter values

ABM simulations can be computationally expensive when the model includes complex rules or consists of many agents. This computational bottleneck makes it challenging to investigate ABM behavior at many parameter values. We now examine how performing multivariate interpolation on several BINN-inferred diffusion rates $\mathcal{D}^{MLP}(T; \mathbf{p})$ can aid the prediction of previously-unseen ABM data at new parameter values (see Section 3.4 for implementation details).

We predict new data from the Adhesion and Pulling & Adhesion ABMs in this section. We do not include the Pulling ABM in this work because the mean-field PDE model accurately forecasted ABM data for all parameter values that we considered in Section 4.2.1.

4.3.1 Predicting Adhesion ABM data

The parameters for the Adhesion ABM are $\mathbf{p} = (r_m^{adh}, p_{adh})^T$. We perform ABM data prediction for $p_{adh} \geq 0.5$ in this section because we found that the mean-field PDE model accurately forecasted ABM data for $p_{adh} \leq 0.5$ in Section 4.2.2.

We first predict ABM data when varying p_{adh} and fixing r_m^{adh} . The prior data collection consists of six ABM datasets generated by varying $p_{adh} = 0.5, 0.6, 0.7, \dots, 1.0$ while fixing $r_m^{adh} = 1.0$; the new data collection consists of five ABM datasets generated by varying $p_{adh} = 0.55, 0.65, 0.75, 0.85,$ and 0.95 while fixing $r_m^{adh} = 1.0$. We performed multivariate interpolation over the six inferred $\mathcal{D}^{MLP}(T; \mathbf{p})$ terms from the prior data collection to generate $\mathcal{D}^{interp}(T; \mathbf{p})$. We use this interpolant to predict the diffusion rates for all

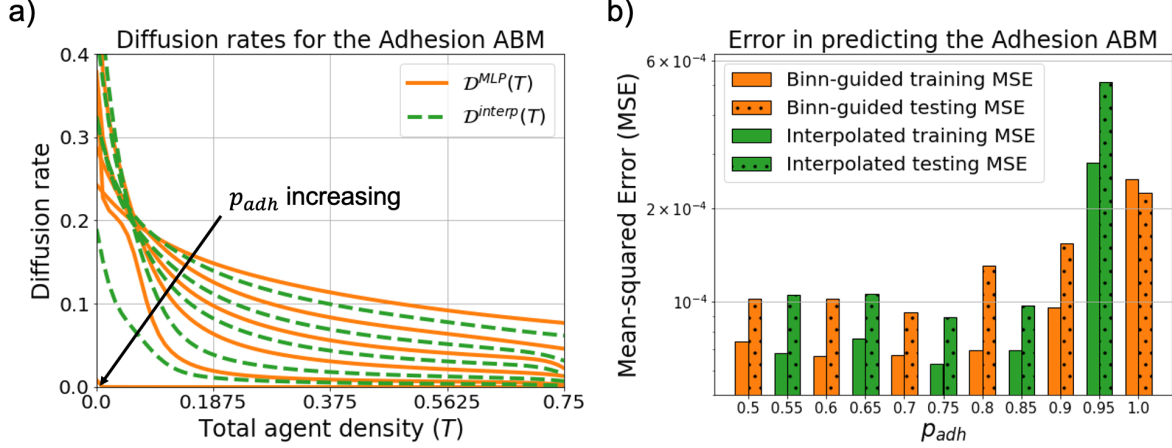


Figure 9: Predicting Adhesion ABM data with BINN-guided PDEs and multivariate interpolation for new p_{adh} values. The parameters for the Adhesion ABM are given by $\mathbf{p} = (r_m^{adh}, p_{adh})^T$. Here, we vary p_{adh} while fixing $r_m^{adh} = 1.0$. The prior data collection consists of $p_{adh} = 0.5, 0.6, \dots, 1.0$ and the new data collection consists of $p_{adh} = 0.55, 0.65, \dots, 0.95$ (a) Plots of the learned $\mathcal{D}^{MLP}(T; \mathbf{p})$ diffusion rates for the prior data collection. We performed multivariate interpolation on these rates to obtain $\mathcal{D}^{interp}(T; \mathbf{p})$, which we plot for the new data collection. (b) Plots of the BINN-guided PDEs’ computed training and testing values on the prior data collection, and the interpolated PDE’s training and testing values on the new data collection.

parameters from the new data collection (Figure 9(a)). All interpolated diffusion rates decrease with agent density and tend to fall with larger p_{adh} values. Most of the computed training and testing MSE values on the new data collection are comparable to their counterparts from the prior data collection (Figure 9(b)). The lone exception occurs at $p_{adh} = 0.95$, where the testing MSE exceeds 5×10^{-4} while the testing MSEs at $p_{adh} = 0.9$ and 1.0 do not exceed 2.5×10^{-4} . Visual inspection of the simulated PDE prediction against ABM data at $p_{adh} = 0.95$ reveals that it matches the data well but slightly mispredicts the data’s heel at later time points (Supplementary Figure 15(a-c)).

We next predict ABM data when varying the r_m^{adh} and p_{adh} parameters. The prior data collection consists of 18 ABM datasets generated by varying $r_m^{adh} = 0.1, 0.5, 1.0$ and $p_{adh} = 0.5, 0.6, \dots, 1.0$; the new data collection consists of ten ABM datasets generated from a latin hypercube sampling of $(r_m^{adh}, p_{adh}) \in [0.1, 1.0] \times [0.5, 1.0]$ (Figure 10(a) and Supplementary Table 5). We performed multivariate interpolation over each $\mathcal{D}^{MLP}(T; \mathbf{p})$ from the prior data collection to generate $\mathcal{D}^{interp}(T; \mathbf{p})$. The predicted diffusion rates for the new data collection decrease with agent density, rise for larger r_m^{adh} values, and decrease faster for larger p_{adh} values (Figure 10(b)). We order the parameters from the new data collection by increasing training MSE values; four of the five lowest training MSE values result from the five smallest p_{adh} values, and four of the five highest MSE values result from the five highest p_{adh} values (Figure 10(c)). The four lowest training and testing MSE values are all below 110^{-4} , the eight lowest are all below 2×10^{-4} , and the highest testing MSE value reaches 1.6×10^{-3} . Visual inspection of the interpolated PDE prediction with the highest testing

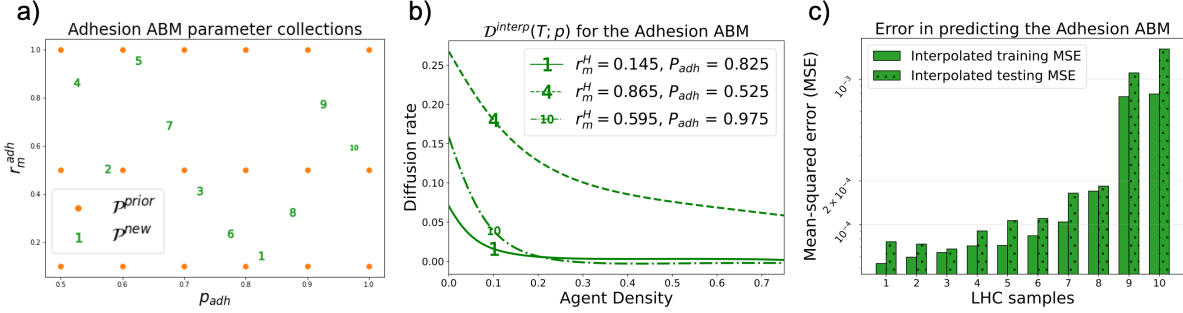


Figure 10: Predicting Adhesion ABM data with BINN-guided PDEs and multivariate interpolation for new r_m^{adh} and p_{adh} values. The parameters for the Adhesion ABM are given by $\mathbf{p} = (r_m^{adh}, p_{adh})^T$. Here, we vary both parameters. (a) The prior data collection consists of $r_m^{adh} = 0.1, 0.5, 1.0$ and $p_{adh} = 0.5, 0.6, \dots, 1.0$ and the new data collection consists of a Latin hypercube (LHC) sampling of $\mathbf{p} \in [0.1, 1.0] \times [0.5, 1.0]$ with 10 samples. (b) We performed multivariate interpolation on the $\mathcal{D}^{MLP}(T; \mathbf{p})$ rates on the prior data collection to obtain $\mathcal{D}^{interp}(T; \mathbf{p})$. We plot three illustrative $\mathcal{D}^{interp}(T; \mathbf{p})$ values from the new data collection. (c) Plots of the interpolated PDE’s training and testing values on the new data collection.

MSE value reveals that this simulation mispredicts the data’s heel but otherwise matches the ABM data well (Supplementary Figure 16(a-c)). Visual inspection of the interpolated PDE prediction with the third-highest MSE value shows that this simulation accurately matches the ABM data (Supplementary Figure 16(d-f)).

4.3.2 Predicting Adhesion & Pulling ABM data

The parameters for the Pulling & Adhesion ABM are $\mathbf{p} = (r_m^{pull}, r_m^{adh}, p_{pull}, p_{adh}, \alpha)^T$. We perform ABM data prediction over a large range of parameter values to determine if the one-compartment BINN-guided PDE simulations can predict this ABM’s data that results from two interacting subpopulations.

We perform multivariate interpolation over the p_{pull}, p_{adh} , and α parameters while fixing $r_m^{pull} = 1.0$ and $r_m^{adh} = 0.25$. The prior and new data collections consist of 40 and 20 ABM parameter combinations, respectively, that were generated from Latin hypercube samplings of $(p_{pull}, p_{adh}, \alpha) \in [0, 0.67] \times [0, 0.67] \times [0, 1]$ (Figure 11(a) and Supplementary Tables 6 and 7). We chose samplings where $p_{pull} + p_{adh} \leq 1.0$ for all samples. The computed training and testing MSE values for the new parameter collection suggest all simulated PDE predictions accurately match the ABM data at those parameters (Figure 11(b)). Of the 20 computed testing MSE values in the new data collection, four are below 1×10^{-4} , 16 are below 2×10^{-4} , and all are below 5×10^{-4} . The highest and third highest testing MSE value results from $(p_{pull}, p_{adh}, \alpha) = (0.218, 0.553, 0.675)$ and $(0.251, 0.486, 0.975)$, respectively. Visually inspecting the interpolated PDE predictions from these parameter values against ABM data reveals that both match the data well, though the worst prediction overpredicts the highest ABM density values (Supplementary Figure 17).

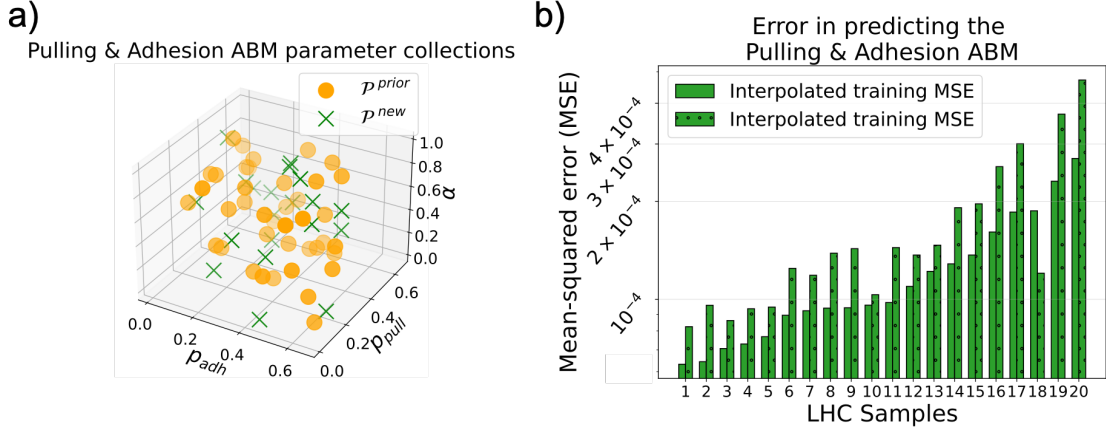


Figure 11: Predicting Pulling & Adhesion ABM data for new p_{pull}, p_{adh} , and α values. The parameters for the Adhesion ABM are given by $\mathbf{p} = (r_m^{adh}, r_m^{pull}, p_{adh}, p_{pull}, \alpha)^T$. Here, we vary p_{pull}, p_{adh} , and α while fixing $r_m^{pull} = 1.0$ and $r_m^{adh} = 0.25$. (a) The prior data consists of a Latin hypercube (LHC) sampling of $(p_{pull}, p_{adh}, \alpha) \in [0, 0.67] \times [0, 0.67] \times [0, 1]$ with 40 samples and the new data consists of a LHC sampling of the same domain with 20 samples. (b) Plots of the interpolated PDE’s training and testing values on the new data, arranged by increasing training MSE values.

4.4 Comparing the computational expense of each modeling approach

We finish with a discussion on the computational expense of all approaches discussed in this work (Table 3 and Supplementary Figure 18). We recorded the computed wall times to simulate each ABM, train each BINN model, and simulate each PDE in Section 4.2. Averaging across all ABMs suggests that the average ABM dataset took 40.0 minutes to generate with a standard deviation of 15.6 minutes. The average mean-field PDE model simulations for the Pulling ABM and the Adhesion ABM took 0.6 and 0.5 seconds to complete, respectively, which are about 4,000 and 4,500 times faster than the average ABM simulations time. The average mean-field PDE model simulation time for the Pulling & Adhesion ABM was 4.7 seconds, which is 542 times faster than the average ABM simulation time. Training a BINN model is the most time-consuming task with an average time of 11.2 hours across all ABMs with a standard deviation of 4.32 hours. The average BINN-guided PDE simulation takes 82.9 seconds with a standard deviation of 77.12 seconds, which is approximately 28 times faster than simulating the ABM.

5 Discussion and Future Work

In this work, we introduced how BINNs can be used to learn BINN-guided PDE models from simulated ABM data. BINN-guided PDE model simulations provide a new approach for forecasting and predicting ABM data. This methodology works by training a BINN model to fit a simulated ABM dataset while also obeying a pre-specified PDE model framework. After model training, future ABM data can be forecasted by simulating

ABM Name	ABM simulation	MF PDE simulation	BINN Training	BG PDE simulation
Adhesion	37.5 (15.4) minutes	0.5 (0.15) seconds	10.6 (4.44) hours	16.9 (23.65) seconds
Pulling	39.9 (15.8) minutes	0.6 (0.20) seconds	10.0 (3.99) hours	164.8 (156.9) seconds
Pulling & Adhesion	42.5 (15.52) minutes	4.7 (1.20) seconds	13.1 (4.54) hours	66.9 (50.81) seconds

Table 3: Computational expenses of each modeling approach. The mean wall time computations (standard deviation in parentheses) for ABM simulations, BINN training, mean-field (MF) PDE simulations, and BINN-guided (BG) PDE simulations for all three ABMs.

the BINN-guided PDE. We predicted ABM data at new parameter values by simulating the pre-specified PDE framework with an interpolated modeling term. This model term is computed by interpolating over several learned BINN model terms that result from a sample of parameter values.

It is challenging to predict how input parameters affect ABMs’ output behavior due to their heavy computational nature. Mathematical modelers often address this limitation by coarse-graining ABM rules into computationally-efficient mean-field DE models. Unfortunately, these DE models may give misleading ABM predictions; furthermore, they can be ill-posed for certain parameter values [1, 8]. Here, we demonstrated that BINN-guided PDE models accurately forecasted future ABM data and predicted ABM data from new parameter values. One benefit of this BINN-guided approach for ABM prediction is that BINNs can, in theory, be trained to simulated data from complex ABMs because BINN models are agnostic to the ABM rules. This is in contrast to the coarse-graining approach, which is limited to ABMs with simple rules to ensure a final PDE model can be recovered.

A limitation of the BINN-guided approach for ABM forecasting and prediction is the computational expense of BINN model training. The average BINN training procedure in this study took 11.2 hours, which is about 17 times longer than the average ABM data generation time of 40 minutes. Once a BINN model has been trained, however, the average BINN-guided PDE simulation took 83 seconds, which is roughly 28 times faster than the average time to generate an ABM dataset. One possible source of these long BINN training times is our chosen BINN model architecture, which consists of over over 50,000 parameters to train. Kaplarevi-Malii et al. [37] proposed a genetic algorithm to identify the optimal model architecture for PINN models. In future work, we plan to implement this algorithm to identify simpler BINN model architectures that can be efficiently trained to learn predictive PDE models for ABMs.

Future work will include developing new BINN model architectures to enhance our understanding of heterogeneous ABMs. In this study, we simulated an ABM with two agent types to model a heterogeneous population and demonstrated that BINNs can learn interpretable one-compartment PDE models to forecast and predict simulated data from this ABM. In a future study, we plan to update the BINN modeling architecture to predict the density of each agent type using a multi-compartment PDE framework with separate model terms for each agent type. This will allow us to interpret how the input model parameters affect the modeling terms for each agent type. We could quantify the uncertainty of each modeling term by

	ABM prediction	Interpretability
Pulling ABM	MF PDE accurate for all parameters BG PDE accurate for all parameters	MF PDE is interpretable BG PDE is interpretable
Adhesion ABM	MF PDE accurate for $p_{adh} \leq 0.5$ BG PDE accurate for $p_{adh} \leq 0.9$	MF PDE is interpretable BG PDE is interpretable
Pulling & Adhesion ABM	MF PDE accurate for all parameters BG PDE accurate for all parameters	MF PDE not interpretable BG PDE is interpretable

Table 4: Highlighting the ability of mean-field (MF) and BINN-guided (BG) PDEs to accurately forecast simulated ABM data with interpretable PDE models.

incorporating the Bayesian inference techniques from [38] into our analysis. There are thus many ways to extend the methods proposed in this work, which will allow us to study more complex ABMs and improve our understanding of the learned DE models.

Case study: collective migration. In this study, we applied the BINN methodology to three case study ABMs, each of which consists of rules on how agent pulling and adhesion impact collective migration. These models (namely, the Pulling ABM, Adhesion ABM, and the Pulling & Adhesion ABM) capture some of the key cellular interactions that drive collective migration during tumor invasion, wound healing, and embryo development [5, 17]. Mean-field and BINN-guided PDE models can be used to forecast and predict simulated data from the three case study ABMs. In addition to predicting ABM output, we can interpret these PDE models by visually inspecting their diffusion rates. In Table 4, we summarize the predictive and interpretative capabilities of both PDE models for the three case study ABMs.

For the Pulling ABM, the trained BINN models learn diffusion rates that are similar to the mean-field PDE diffusion rates for all parameter values (Figures 5(a) and (c)). As a result, both models perform similarly in forecasting future ABM data (Figures 5(b) and (d)). The diffusion rates from both approaches propose that population diffusion increases with agent density, the rate of agent migration, and the probability of agent pulling.

For the Adhesion ABM, both PDE models are able to accurately forecast ABM data for adhesion probabilities below 0.5 (Figure 6(b) and (d)). The mean-field PDE’s predictions become worse when this probability exceeds 0.5, however, and this model is ill-posed when this probability exceeds 0.75. BINN-guided PDEs, on the other hand, are well-posed for all adhesion probabilities, and their ABM forecasts and predictions are accurate when this probability is below 0.9 (Figures 6(b) and (d), 9(b), and 10(c)). The diffusion rates from both PDEs agree that population diffusion decreases when either agent density or the probability of agent adhesion increases (Figure 6(a) and (c)). The BINN-guided PDE proposes that population diffusion decreases with agent density faster than the mean-field PDE suggests. Both models suggest that population diffusion increases with the rate of adhesive agent migration.

For the Pulling & Adhesion ABM, both PDE models accurately forecast the total ABM data for most

parameter values considered (Figure 8). The BINN-guided PDE achieves this high accuracy with a one-compartment PDE model; this PDE’s diffusion rate describes how the total population diffuses. We found that many (but not all) learned diffusion rates are U-shaped, meaning that agent diffusion decreases with agent density at low density values and increases at high density values (Figure 7). Visualizing the learned diffusion rates for many parameter values reveals that this U-shape increases when we increase the rates of pulling agent migration, adhesive agent migration, and the probability of agent pulling; the U-shape decreases when we increase the probability of adhesion or the proportion of adhesive agents in the simulation. As opposed to the BINN-guided PDE model, the mean-field PDE for this ABM contains two compartments, one for pulling agents and another for adhesive agents. This PDE model is quite complex and comprised of many terms. As a result, it is not easy to interpret how this PDE model changes with model parameters.

In future work, we plan to study more complex ABMs of collective migration using the BINNs methodology. Chappelle and Yates [12] considered rules where multiple agents interact during cell pulling events. They found that the predictive accuracy of mean-field PDE models declines as more agents become involved in pulling processes. In our study, we focused on simple cell-cell interaction rules between two agents: in future work, we will investigate how BINN-guided PDEs change with the number of agents involved in each interaction. Gallaher et al. [51] used a complex two-dimensional spatial ABM to study how spatial heterogeneity and evolutionary dynamics impact a tumor’s response to adaptive cancer therapies. Each agent in their model has its own internal growth rate and response to drug exposure. It would be interesting to determine if the BINNs approach from our study can be used to describe the complex spread, growth, and sensitivity of this model’s simulated tumors in response to drug treatment. Agent proliferation is an important component of collective migration that we did not consider in our study. Many previous studies have shown that coarse-grained DE models fail to accurately describe ABM simulations when agents proliferate quickly [8]. It would be straightforward to extend our methods to predict ABM data from models where agents migrate and proliferate by adding a population growth term into the PDE framework during BINN training.

Acknowledgements: The author thanks R. Baker, J. Gevertz, K. Flores, and S. Nardini for helpful discussions and commentary.

Data Availability statement: All code and simulated data for this work is publicly available at https://github.com/johnnardini/Forecasting_predicting_ABMs.

Conflict of interest: The author declares no conflict of interest

Funding Statement: The author acknowledges use of the ELSA high performance computing cluster at The College of New Jersey for conducting the research reported in this paper. This cluster is funded in part by the National Science Foundation under grant numbers OAC-1826915 and OAC-1828163.

References

- [1] Kathleen Anguige and Christian Schmeiser. A one-dimensional model of cell diffusion and aggregation, incorporating volume filling and cell-to-cell adhesion. *Journal of Mathematical Biology*, 58(3):395, March 2009.
- [2] Fred Brauer, Carlos Castillo-Chavez, and Zhilan Feng. *Mathematical models in epidemiology*, volume 69 of *Texts in Applied Mathematics*. Springer, New York, NY, 2019.
- [3] Theo Gibbs, Simon A. Levin, and Jonathan M. Levine. Coexistence in diverse communities with higher-order interactions. *Proceedings of the National Academy of Sciences*, 119(43):e2205063119, October 2022. Publisher: Proceedings of the National Academy of Sciences.
- [4] A. Huppert and G. Katriel. Mathematical modelling and prediction in infectious disease epidemiology. *Clinical Microbiology and Infection*, 19(11):999–1005, November 2013.
- [5] John T. Nardini, Douglas A. Chapnick, Xuedong Liu, and David M. Bortz. Modeling keratinocyte wound healing: cell-cell adhesions promote sustained migration. *Journal of Theoretical Biology*, 400:103–117, July 2016.
- [6] Shahzeb Raja Noureen, Jennifer P. Owen, Richard L. Mort, and Christian A. Yates. Swapping in lattice-based cell migration models. *Physical Review E*, 107(4):044402, April 2023.
- [7] Yanni Xiao and Lansun Chen. Modeling and analysis of a predator–prey model with disease in the prey. *Mathematical Biosciences*, 171(1):59–82, May 2001.
- [8] Ruth E. Baker and Matthew J. Simpson. Correcting mean-field approximations for birth-death-movement processes. *Physical Review E*, 82(4):041905, October 2010.
- [9] Volker Grimm, Eloy Revilla, Uta Berger, Florian Jeltsch, Wolf M. Mooij, Steven F. Railsback, Hans-Hermann Thulke, Jacob Weiner, Thorsten Wiegand, and Donald L. DeAngelis. Pattern-oriented modeling of agent-based complex systems: lessons from ecology. *Science*, 310(5750):987–991, November 2005. Publisher: American Association for the Advancement of Science.
- [10] Brandon D. L. Marshall and Sandro Galea. Formalizing the role of agent-based modeling in causal inference and epidemiology. *American Journal of Epidemiology*, 181(2):92–99, January 2015.
- [11] Melissa Tracy, Magdalena Cerdá, and Katherine M. Keyes. Agent-based modeling in public health: current applications and future directions. *Annual Review of Public Health*, 39(1):77–94, 2018. _eprint: <https://doi.org/10.1146/annurev-publhealth-040617-014317>.
- [12] George Chappelle and Christian A. Yates. Pulling in models of cell migration. *Physical Review E*, 99(6):062413, June 2019.

- [13] Matthew J. Simpson, Ruth E. Baker, Pascal R. Buenzli, Ruanui Nicholson, and Oliver J. Maclaren. Reliable and efficient parameter estimation using approximate continuum limit descriptions of stochastic models. *Journal of Theoretical Biology*, 549:111201, September 2022.
- [14] John T. Nardini, Ruth E. Baker, Matthew J. Simpson, and Kevin B. Flores. Learning differential equation models from stochastic agent-based model simulations. *Journal of The Royal Society Interface*, 18(176):rsif.2020.0987, 20200987, March 2021.
- [15] Le-Minh Kieu, Nicolas Malleson, and Alison Heppenstall. Dealing with uncertainty in agent-based models for short-term predictions. *Royal Society Open Science*, 7(1):191074, January 2020.
- [16] Dale Larie, Gary An, and R. Chase Cockrell. The use of artificial neural networks to forecast the behavior of agent-based models of pathophysiology: an example utilizing an agent-based model of sepsis. *Frontiers in Physiology*, 12:716434, October 2021.
- [17] Robin N. Thompson, Christian A. Yates, and Ruth E. Baker. Modelling cell migration and adhesion during development. *Bulletin of Mathematical Biology*, 74(12):2793–2809, December 2012.
- [18] Stuart T. Johnston, Matthew J. Simpson, and Ruth E. Baker. Mean-field descriptions of collective migration with strong adhesion. *Physical Review E*, 85(5):051922, May 2012.
- [19] Matthew J. Simpson, Jesse A. Sharp, and Ruth E. Baker. Distinguishing between mean-field, moment dynamics and stochastic descriptions of birth–death–movement processes. *Physica A: Statistical Mechanics and its Applications*, 395:236–246, February 2014.
- [20] Daniel J. VandenHeuvel, Pascal R. Buenzli, and Matthew J. Simpson. Pushing coarse-grained models beyond the continuum limit using equation learning, August 2023. arXiv:2308.11086 [math, q-bio].
- [21] Steven L. Brunton, Joshua L. Proctor, and J. Nathan Kutz. Discovering governing equations from data by sparse identification of nonlinear dynamical systems. *Proceedings of the National Academy of Sciences*, 113(15):3932–3937, April 2016.
- [22] E. Kaiser, J. Nathan Kutz, and Steven L. Brunton. Sparse identification of nonlinear dynamics for model predictive control in the low-data limit. *Proceedings of the Royal Society A: Mathematical, Physical and Engineering Sciences*, 474(2219):20180335, November 2018.
- [23] Samuel Rudy, Alessandro Alla, Steven L. Brunton, and J. Nathan Kutz. Data-driven identification of parametric partial differential equations. *SIAM Journal on Applied Dynamical Systems*, 18(2):643–660, January 2019. Publisher: Society for Industrial and Applied Mathematics.
- [24] Kathleen Champion, Bethany Lusch, J. Nathan Kutz, and Steven L. Brunton. Data-driven discovery of coordinates and governing equations. *Proceedings of the National Academy of Sciences*, 116(45):22445–22451, November 2019. Publisher: National Academy of Sciences Section: Physical Sciences.

- [25] Niall M. Mangan, Steven L. Brunton, Joshua L. Proctor, and J. Nathan Kutz. Inferring biological networks by sparse identification of nonlinear dynamics. *IEEE Transactions on Molecular, Biological and Multi-Scale Communications*, 2(1):52–63, June 2016. Conference Name: IEEE Transactions on Molecular, Biological and Multi-Scale Communications.
- [26] Niall M. Mangan, J. Nathan Kutz, Steven L. Brunton, and Joshua L. Proctor. Model selection for dynamical systems via sparse regression and information criteria. *Proceedings of the Royal Society A: Mathematical, Physical and Engineering Sciences*, 473(2204):20170009, August 2017.
- [27] Daniel A. Messenger and David M. Bortz. Weak SINDy: galerkin-based data-driven model selection. *Multiscale Modeling & Simulation*, 19(3):1474–1497, January 2021.
- [28] Daniel A. Messenger and David M. Bortz. Weak SINDy for partial differential equations. *Journal of Computational Physics*, 443:110525, October 2021.
- [29] John H. Lagergren, John T. Nardini, G. Michael Lavigne, Erica M. Rutter, and Kevin B. Flores. Learning partial differential equations for biological transport models from noisy spatio-temporal data. *Proceedings of the Royal Society A: Mathematical, Physical and Engineering Sciences*, 476(2234):20190800, February 2020.
- [30] John H. Lagergren, John T. Nardini, Ruth E. Baker, Matthew J. Simpson, and Kevin B. Flores. Biologically-informed neural networks guide mechanistic modeling from sparse experimental data. *PLOS Computational Biology*, 16(12):e1008462, December 2020. Publisher: Public Library of Science.
- [31] John T. Nardini, John H. Lagergren, Andrea Hawkins-Daarud, Lee Curtin, Bethan Morris, Erica M. Rutter, Kristin R. Swanson, and Kevin B. Flores. Learning equations from biological data with limited time samples. *Bulletin of Mathematical Biology*, 82(9):119, September 2020.
- [32] Samuel H. Rudy, Steven L. Brunton, Joshua L. Proctor, and J. Nathan Kutz. Data-driven discovery of partial differential equations. *Science Advances*, 3(4):e1602614, April 2017. Publisher: American Association for the Advancement of Science Section: Research Article.
- [33] Daniel A. Messenger, Graycen E. Wheeler, Xuedong Liu, and David M. Bortz. Learning anisotropic interaction rules from individual trajectories in a heterogeneous cellular population. *Journal of The Royal Society Interface*, 19(195):20220412, October 2022.
- [34] Daniel A. Messenger and David M. Bortz. Learning mean-field equations from particle data using WSINDy. *Physica D: Nonlinear Phenomena*, 439:133406, November 2022.
- [35] Rohit Supekar, Boya Song, Alasdair Hastewell, Gary P. T. Choi, Alexander Mietke, and Jörn Dunkel. Learning hydrodynamic equations for active matter from particle simulations and experiments. *Proceedings of the National Academy of Sciences*, 120(7):e2206994120, February 2023.

- [36] Shengze Cai, Zhicheng Wang, Sifan Wang, Paris Perdikaris, and George Em Karniadakis. Physics-informed neural networks for heat transfer Problems. *Journal of Heat Transfer*, 143(6):060801, June 2021.
- [37] Ana Kaplarević-Mališić, Branka Andrijević, Filip Bojović, Srđan Nikolić, Lazar Krstić, Boban Stojanović, and Miloš Ivanović. Identifying optimal architectures of physics-informed neural networks by evolutionary strategy. *Applied Soft Computing*, page 110646, July 2023.
- [38] Kevin Linka, Amelie Schäfer, Xuhui Meng, Zongren Zou, George Em Karniadakis, and Ellen Kuhl. Bayesian physics informed neural networks for real-world nonlinear dynamical systems. *Computer Methods in Applied Mechanics and Engineering*, 402:115346, December 2022.
- [39] M. Raissi, P. Perdikaris, and G.E. Karniadakis. Physics-informed neural networks: a deep learning framework for solving forward and inverse problems involving nonlinear partial differential equations. *Journal of Computational Physics*, 378:686–707, February 2019.
- [40] Yeonjong Shin, Jerome Darbon, and George Em Karniadakis. On the convergence of physics informed neural networks for linear second-order elliptic and parabolic type PDEs. *Communications in Computational Physics*, 28(5):2042–2074, June 2020. arXiv: 2004.01806.
- [41] Marc C. Kennedy and Anthony O’Hagan. Bayesian calibration of computer models. *Journal of the Royal Statistical Society Series B: Statistical Methodology*, 63(3):425–464, September 2001.
- [42] Sushant S. Garud, Iftekhar A. Karimi, and Markus Kraft. Design of computer experiments: a review. *Computers & Chemical Engineering*, 106:71–95, November 2017.
- [43] Ralph C. Smith. *Uncertainty quantification: theory, implementation, and applications*. Society for Industrial and Applied Mathematics, Philadelphia, PA, January 2013.
- [44] Jari Kaipio and Ville Kolehmainen. Approximate marginalization over modelling errors and uncertainties in inverse problems. In Paul Damien, Petros Dellaportas, Nicholas G. Polson, and David A. Stephens, editors, *Bayesian Theory and Applications*, pages 644–672. Oxford University Press, January 2013.
- [45] Jari P. Kaipio and Erkki Somersalo. *Statistical and computational inverse problems*, volume 160 of *Applied Mathematical Sciences*. Springer New York, New York, NY, 2005.
- [46] Jari Kaipio and Erkki Somersalo. Statistical inverse problems: discretization, model reduction and inverse crimes. *Journal of Computational and Applied Mathematics*, 198(2):493–504, January 2007.
- [47] Claudio Angione, Eric Silverman, and Elisabeth Yaneske. Using machine learning as a surrogate model for agent-based simulations. *PLOS ONE*, 17(2):e0263150, February 2022.
- [48] Abdul Afram and Farrokh Janabi-Sharifi. Black-box modeling of residential HVAC system and comparison of gray-box and black-box modeling methods. *Energy and Buildings*, 94:121–149, May 2015.

- [49] Michalina Janiszewska, Marina C. Primi, and Tina Izard. Cell adhesion in cancer: beyond the migration of single cells. *Journal of Biological Chemistry*, 295(8):2495–2505, February 2020.
- [50] Katheryn E. Rothenberg, Yujun Chen, Jocelyn A. McDonald, and Rodrigo Fernandez-Gonzalez. Rap1 coordinates cell-cell adhesion and cytoskeletal reorganization to drive collective cell migration in vivo. *Current Biology*, 33(13):2587–2601.e5, July 2023.
- [51] Jill A. Gallaher, Pedro M. Enriquez-Navas, Kimberly A. Luddy, Robert A. Gatenby, and Alexander R.A. Anderson. Spatial heterogeneity and evolutionary dynamics modulate time to recurrence in continuous and adaptive cancer therapies. *Cancer Research*, 78(8):2127–2139, April 2018.
- [52] Alexander Kurganov and Eitan Tadmor. New high-resolution central schemes for nonlinear conservation laws and convection–diffusion equations. *Journal of Computational Physics*, 160(1):241–282, May 2000.
- [53] Linda Petzold. Automatic selection of methods for solving stiff and nonstiff systems of ordinary differential equations. *SIAM Journal on Scientific and Statistical Computing*, 4(1):136–148, March 1983.

A ABM Rules

A.1 The Pulling Model

The Pulling model consists of pulling agents that migrate with rate³ r_m^{pull} and perform rules A and B from Figure 1. Suppose a pulling agent at lattice site (i, j) chooses to move rightwards into site $(i + 1, j)$. If the lattice site $(i - 1, j)$ is unoccupied, then the agent performs Rule A and moves into site $(i + 1, j)$. If the lattice site $(i - 1, j)$ is occupied, then the agent attempts Rule B on agent pulling. This event succeeds with probability p_{pull} , and the agent moves to site $(i + i, j)$ and pulls its neighbor into lattice site (i, j) . This event fails with probability $1 - p_{pull}$, in which the agent moves into site $(i + i, j)$ but the neighbor remains at lattice site $(i, j - 1)$. These rules can be described by the following trimolecular reaction rates:



Equivalent reactions govern agent migration and pulling in the other three directions.

A.2 The Adhesion Model

The Adhesion model consists of adhesive agents that migrate with rate r_m^{adh} and perform rules C and D from Figure 1. Suppose an adhesive agent at lattice site (i, j) chooses to move rightwards into site $(i + 1, j)$. If the lattice site $(i - 1, j)$ is unoccupied, then the agent performs Rule C and moves into site $(i + 1, j)$. If the lattice site $(i - 1, j)$ is occupied, then the neighboring agent attempts Rule D to adhere to the migrating agent and abort their movement. This event succeeds with probability p_{adh} , and neither agent changes its location. This adhesion event fails with probability $1 - p_{adh}$, and the migrating agent moves to site $(i + i, j)$ and the neighbor remains at lattice site $(i, j - 1)$. These rules can be described by the following trimolecular reaction rates:



A.3 The Pulling & Adhesion Model

The Pulling & Adhesion model consists of both pulling and adhesive agents. This model implements Rules A-F from Figure 1. Rules A-D are unchanged from their descriptions in Sections A.1 and A.2. If a pulling agent at lattice site (i, j) chooses to move rightwards into site $(i + 1, j)$ while an adhesive agent occupies site

³Meaning that pulling agents attempt to migrate over an infinitesimal time interval of length dt with probability $r_m^{pull}dt$.

$(i - i, j)$, then Rule E dictates the agents' attempts to pull and adhere to each other. The migrating pulling agent succeeds with probability p_{pull} and moves to site $(i + 1, j)$ while pulling the neighboring adhesive agent into site (i, j) ; the neighboring adhesive agent successfully aborts the pulling agent's migration event with probability p_{adh} ; both agents fail with probability $1 - p_{adh} - p_{pull}$ and the pulling agent moves to site $(i + 1, j)$ while the adhesive agent remains at site $(i - 1, j)$. Based on our definition of this rule, it is not possible that both the pulling and adhesion events succeed, so the parameters must satisfy $0 \leq p_{pull} + p_{adh} \leq 1$. Rule E can be described by the following trimolecular reaction rate:



If an adhesive agent at lattice site (i, j) chooses to move rightwards into site $(i + 1, j)$ while a pulling agent occupies site $(i - i, j)$, then Rule F dictates that the adhesive agent moves into site $(i + 1, j)$ and the pulling agent remains at site $(i - 1, j)$. Rule F can be described by the following trimolecular reaction rate:



B ABM implementation

Each model is simulated in the spatial domain $(x, y) \in [0, X] \times [0, Y]$. We choose $X = 200$ and $Y = 40$ to represent a thin rectangle where collective migration primarily occurs along the x -dimension and is not affected by the boundary in this dimension. We represent this space with a two-dimensional lattice with square lattice sites with length $\Delta = 1$ to imitate a typical cell length. The $(i, j)^{\text{th}}$ lattice site is centered at (x_i, y_j) , where $x_i = (i - 0.5)\Delta$, $i = 1, \dots, X$, and $y_j = (j - 0.5)\Delta$, $j = 1, \dots, Y$. Each model is an exclusion process, meaning that each agent can only occupy one lattice site at a time, and each lattice site is occupied by at most one agent. The parameter $\alpha \in (0, 1)$ denotes the proportion of nonempty lattice sites that are occupied by adhesive agents in the simulation, and $(1 - \alpha)$ denotes the proportion of nonempty lattice sites that are occupied by pulling agents in the simulation.

All model simulations are initialized by populating 75% of the lattice sites in the middle 20% of columns, e.g., 75% of the lattice sites in $\{(x_i, y_j)\}_{j=1}^Y$ are initially occupied for $i = 80, \dots, 120$. All other columns are initially empty. Reflecting boundary conditions are used at the boundaries of lattice to enforce a no-flux condition in the spatial domain. We simulate each ABM using the Gillespie algorithm, which we provide for the Pulling & Adhesion ABM in Supplementary Algorithm 1 in appendix C. All ABMs are simulated until $t = 1000$.

C Gillespie algorithm

Our implementation of the Gillespie Algorithm for the Pulling & Adhesion ABM is provided in Supplementary Algorithm 1.

Algorithm 1: Gillespie algorithm for the Pulling & Adhesion ABM

```

Create an  $X \times Y$  lattice with user-specified placement of agents
Set  $t = 0$ 
Set maximum simulation time  $t_{\text{end}}$ 
Set  $P(t)$  and  $H(t)$  equal to the number of Pulling and Adhesive agents on the lattice, respectively
while  $t < t_{\text{end}}$  do
    Calculate the following random variables, uniformly distributed on  $[0, 1]$ :  $\gamma_1, \gamma_2$ 
    Calculate the propensity function  $a(t) = r_m^{\text{pull}}P(t) + r_m^{\text{adh}}H(t)$ 
    Calculate time step  $\tau = -\ln(\gamma_1)/a(t)$ 
     $t = t + \tau$ 
     $R = a(t)\gamma_2$ 
    if  $R < r_m^{\text{pull}}P(t)$  then
        | Perform Pulling agent migration (Supplementary Algorithm 2)
    else if  $R < r_m^{\text{pull}}P(t) + r_m^{\text{adh}}H(t)$  then
        | Perform Adhesive agent migration (Supplementary Algorithm 3)
end

```

D Coarse-graining ABM rules into PDE models

We will coarse-grain the Pulling, Adhesion, and Pulling & Adhesion ABMs into their mean-field PDE models. Each ABM consists of a combination of Rules A-F from Figure 1. Each rule updates the occupancies of three consecutive lattice sites, such as $\{(i, j-1), (i, j), (i, j+1)\}$. Let the variables $P_{i,j}(t)$, $H_{i,j}(t)$, and $0_{i,j}(t)$ denote the probabilities that lattice site (i, j) is occupied by a pulling agent, adhesive agent, or empty at time t , respectively. To convert each rule into a PDE model, we invoke the *mean-field assumption*, which supposes that all lattice site occupancies are independent of each other. This assumption simplifies model coarse-graining by allowing us to replace the joint probability of three lattice site occupancies with the product of the three individual lattice site occupancy probabilities. For example, under the mean-field assumption, we can write the probability that lattice sites $(i, j-1)$, (i, j) , and $(i, j+1)$ are all occupied by pulling agents at time t as $P_{i,j-1}(t)P_{i,j}(t)P_{i,j+1}(t)$; otherwise, we must consider the joint occupancy probability for this triplet of lattice sites. Mean-field DE models can poorly predict ABM behavior when the mean-field assumption is violated during ABM simulations, see [8, 13, 14] for further details.

Algorithm 2: Pulling Agent migration

Randomly choose a pulling agent and determine its lattice site index, $\vec{x} = (i, j)^T$

Choose one of the four cardinal migration directions,

$\vec{d}x = (dx, dy)^T \in \{(1, 0)^T, (-1, 0)^T, (0, 1)^T, (0, -1)^T\}$, with equal probability, 1/4. The neighboring direction is given by $\hat{d}x = -\vec{d}x$

if $\vec{x} + \vec{d}x$ *is empty* **then**

if $\vec{x} + \hat{d}x$ *is empty* **then**

 /* Rule A

*/

 Move the chosen pulling agent to lattice site $\vec{x} + \vec{d}x$

else if $\vec{x} + \hat{d}x$ *is occupied by a Pulling agent* **then**

 /* Rule B

*/

 Calculate the random variable, γ_3 , uniformly distributed on $[0, 1]$

if $\gamma_3 \leq p_{pull}$ **then**

 Move the chosen pulling agent to lattice site $\vec{x} + \vec{d}x$

 Move the neighboring agent to lattice site \vec{x}

else if $\gamma_3 > p_{pull}$ **then**

 Move the chosen pulling agent to lattice site $\vec{x} + \vec{d}x$

else if $\vec{x} + \hat{d}x$ *is occupied by an Adhesive agent* **then**

 /* Rule E

*/

 Calculate the random variable, γ_3 , uniformly distributed on $[0, 1]$

if $\gamma_3 \leq p_{pull}$ **then**

 Move the chosen pulling agent to lattice site $\vec{x} + \vec{d}x$

 Move the neighboring agent to lattice site \vec{x}

else if $\gamma_3 \leq p_{pull} + 1 - p_{adh}$ **then**

 Move the chosen pulling agent to lattice site $\vec{x} + \vec{d}x$

Algorithm 3: Adhesive agent migration

Randomly choose an adhesive agent and determine its lattice site index, $\vec{x} = (i, j)^T$

Choose one of the four cardinal migration directions,

$\vec{dx} = (dx, dy)^T \in \{(1, 0)^T, (-1, 0)^T, (0, 1)^T, (0, -1)^T\}$, with equal probability, $1/4$. The neighboring direction is given by $\hat{dx} = -\vec{dx}$

if $\vec{x} + \vec{dx}$ *is empty* **then**

if $\vec{x} + \hat{dx}$ *is empty* **then**

 /* Rule C

*/

 Move the chosen adhesive agent to lattice site $\vec{x} + \vec{dx}$

else if $\vec{x} + \hat{dx}$ *is occupied by an adhesive agent* **then**

 /* Rule D

*/

 Calculate the random variable, γ_3 , uniformly distributed on $[0, 1]$

if $\gamma_3 \leq (1 - p_{adh})$ **then**

 Move the chosen adhesive agent to lattice site $\vec{x} + \vec{dx}$

else if $\vec{x} + \hat{dx}$ *is occupied by a Pulling agent* **then**

 /* Rule F

*/

 Move the chosen adhesive agent to lattice site $\vec{x} + \vec{dx}$

D.1 Coarse-graining the Pulling ABM

The Pulling ABM is composed of Rules A and B from Figure 1 and Section A.1. We begin coarse-graining this ABM into a PDE model by writing the master equation governing how $P_{i,j}(t)$ changes according to these rules:

$$\frac{\partial P_{i,j}(t)}{\partial t} = K^{Rule\ A} + K^{Rule\ B.1} + K^{Rule\ B.2}. \quad (7)$$

Rule A specifies how pulling agents migrate into an empty lattice site with rate $r_m^{pull}/4$ when there is no neighboring agent in the lattice site opposite the direction of migration. This rate is divided by four because the agent randomly chooses to attempt to migrate into one of its four neighboring lattice sites. We write this rule in the master equation as:

$$\begin{aligned} K^{Rule\ A} = & -\frac{2r_m^{pull}}{4} [0_{i,j-1}(t)P_{i,j}(t)0_{i,j+1}(t) + 0_{i-1,j}(t)P_{i,j}(t)0_{i+1,j}(t)] \\ & + \frac{r_m^{pull}}{4} [0_{i,j-2}(t)P_{i,j-1}(t)0_{i,j}(t) + 0_{i,j}P_{i,j+1}0_{i,j+2} + 0_{i-2,j}P_{i-1,j}0_{i,j} + 0_{i,j}P_{i+1,j}0_{i+2,j}], \end{aligned} \quad (8)$$

where the first line describes how a pulling agent moves out of lattice site (i, j) , and the second line describes how a pulling agent moves into lattice site (i, j) .

Rule B.1 specifies how a pulling agent migrates into an empty neighboring lattice site and pulls its

neighbor along with it, which occurs with probability p_{pull} . We write this rule in the master equation as:

$$\begin{aligned}
K^{Rule\ B.1} = & -\frac{p_{pull}r_m^{pull}}{4} \left[P_{i,j}(t)P_{i,j+1}(t)0_{i,j+2}(t) + 0_{i,j-2}(t)P_{i,j-1}(t)P_{i,j}(t) + \right. \\
& \left. P_{i,j}(t)P_{i+1,j}(t)0_{i+2,j}(t) + 0_{i-2,j}(t)P_{i-1,j}(t)P_{i,j}(t) \right] \\
& + \frac{p_{pull}r_m^{pull}}{4} \left[P_{i,j-2}(t)P_{i,j-1}(t)0_{i,j}(t) + 0_{i,j}(t)P_{i,j+1}(t)P_{i,j+2}(t) + \right. \\
& \left. P_{i-2,j}(t)P_{i-1,j}(t)0_{i,j}(t) + 0_{i,j}(t)P_{i+1,j}(t)P_{i+2,j}(t) \right]. \tag{9}
\end{aligned}$$

Rule B.2 specifies how a pulling agent migrates into an empty neighboring lattice site and fails to pull its neighbor along with it, which occurs with probability $1 - p_{pull}$. We write this rule in the master equation as:

$$\begin{aligned}
K^{Rule\ B.2} = & -\frac{(1-p_{pull})r_m^{pull}}{4} \left[P_{i,j-1}(t)P_{i,j}(t)0_{i,j+1}(t) + 0_{i,j-1}(t)P_{i,j}(t)P_{i,j+1}(t) + \right. \\
& \left. P_{i-1,j}(t)P_{i,j}(t)0_{i+1,j+1}(t) + 0_{i,j-1}(t)P_{i,j}(t)P_{i+1,j}(t) \right] \\
& + \frac{(1-p_{pull})r_m^{pull}}{4} \left[P_{i,j-2}(t)P_{i,j-1}(t)0_{i,j}(t) + 0_{i,j}(t)P_{i,j+1}(t)P_{i,j+2}(t) + \right. \\
& \left. P_{i-2,j}(t)P_{i-1,j}(t)0_{i,j}(t) + 0_{i,j}(t)P_{i+1,j}(t)P_{i+2,j}(t) \right]. \tag{10}
\end{aligned}$$

To obtain the resulting PDE model for the Pulling ABM, we substitute Equations (8), (9), and (10) into Equation (7) and set $0_{i,j} = 1 - P_{i,j}$. We replace each term with its Taylor expansion, up to second order:

$$\begin{aligned}
P_{i\pm m,j}(t) &= P_{i,j}(t) \pm m\Delta(P_{i,j}(t))_x + \frac{m\Delta^2}{2}(P_{i,j}(t))_{xx} + \mathcal{O}(\Delta^3), & m = -2, -1, 0, 1, 2; \\
P_{i,j\pm n}(t) &= P_{i,j}(t) \pm n\Delta(P_{i,j}(t))_y + \frac{n\Delta^2}{2}(P_{i,j}(t))_{yy} + \mathcal{O}(\Delta^3), & n = -2, -1, 0, 1, 2; \tag{11}
\end{aligned}$$

where subscripts denote differentiation with respect to the shown variable, and Δ is the length of each lattice site. As shown in the Mathematica notebook **Pulling_model_coarse_graining.nb**, taking the limit of the resulting expression as $\Delta \rightarrow 0$ leads to the mean-field PDE model for the Pulling ABM:

$$\frac{\partial P}{\partial t} = \nabla \cdot \left(\frac{r_m^{pull}}{4} (1 + 3p_{pull}P^2) \nabla P \right), \tag{12}$$

where $P = P_{i,j}(t)$.

D.2 Coarse-graining the Adhesion ABM

The Adhesion ABM is composed of Rules C and D from Figure 1 and Section A.2. We begin coarse-graining this ABM into a PDE model by writing the master equation governing how $H_{i,j}(t)$ changes according to these rules:

$$\frac{\partial H_{i,j}(t)}{\partial t} = K^{Rule\ C} + K^{Rule\ D}. \tag{13}$$

Rule C specifies how adhesive agents migrate into an empty lattice site with rate $r_m^{adh}/4$ when there is no neighboring agent in the lattice site opposite the direction of migration. We write this rule in the master

equation as:

$$\begin{aligned}
K^{Rule\ C} = & -\frac{2r_m^{adh}}{4} \left[0_{i,j-1}(t)H_{i,j}(t)0_{i,j+1}(t) + 0_{i-1,j}(t)H_{i,j}(t)0_{i+1,j}(t) \right] \\
& + \frac{r_m^{adh}}{4} \left[0_{i,j-2}(t)H_{i,j-1}(t)0_{i,j}(t) + 0_{i,j}(t)H_{i,j+1}(t)0_{i,j+2}(t) + \right. \\
& \left. 0_{i-2,j}(t)H_{i-1,j}(t)0_{i,j}(t) + 0_{i,j}(t)H_{i+1,j}(t)0_{i+2,j}(t) \right], \tag{14}
\end{aligned}$$

where the first line describes how an adhesive agent moves out of lattice site (i, j) , and the second and third lines describe how an adhesive agent moves into lattice site (i, j) .

Rule D specifies how adhesive agents migrate into an empty neighboring lattice site when a neighboring adhesive agent is in the lattice site opposite the direction of migration. The neighboring adhesive agent attempts to adhere to the migrating agent and abort the migration event. The adhesion event succeeds with probability p_{adh} , and neither agent changes its position. The adhesion event fails with probability $1 - p_{adh}$, and the migrating agent shifts into the previously-empty lattice site while the neighboring agent remains in its previous lattice site. We write this rule in the master equation as:

$$\begin{aligned}
K^{Rule\ D} = & -\frac{(1-p_{adh})r_m^{adh}}{4} \left[H_{i,j-1}(t)H_{i,j}(t)0_{i,j+1}(t) + 0_{i,j-1}(t)H_{i,j}(t)H_{i,j+1}(t) + \right. \\
& \left. H_{i-1,j}(t)H_{i,j}(t)0_{i+1,j}(t) + 0_{i-1,j}(t)H_{i,j}(t)H_{i+1,j}(t) \right] \\
& + \frac{(1-p_{adh})r_m^{adh}}{4} \left[H_{i,j-2}(t)H_{i,j-1}(t)0_{i,j}(t) + 0_{i,j}(t)H_{i,j+1}(t)H_{i,j+2}(t) + \right. \\
& \left. H_{i-2,j}(t)H_{i-1,j}(t)0_{i,j}(t) + 0_{i,j}(t)H_{i+1,j}(t)H_{i+2,j}(t) \right]. \tag{15}
\end{aligned}$$

To obtain the resulting PDE model for the Adhesion ABM, we substitute Equations (14) and (15) into Equation (13) and set $0_{i,j} = 1 - H_{i,j}$. We replace each term with its Taylor expansion, up to second order:

$$\begin{aligned}
H_{i\pm m,j}(t) &= H_{i,j}(t) \pm m\Delta(H_{i,j}(t))_x + \frac{m\Delta^2}{2}(H_{i,j}(t))_{xx} + \mathcal{O}(\Delta^3), & m = -2, -1, 0, 1, 2; \\
H_{i,j\pm n}(t) &= H_{i,j}(t) \pm n\Delta(H_{i,j}(t))_y + \frac{n\Delta^2}{2}(H_{i,j}(t))_{yy} + \mathcal{O}(\Delta^3), & n = -2, -1, 0, 1, 2. \tag{16}
\end{aligned}$$

As shown in the Mathematica notebook **Adhesion_model_coarse_graining.nb**, taking the limit of the resulting expression as $\Delta \rightarrow 0$ leads to the mean-field PDE model for the Adhesion ABM:

$$\frac{\partial H}{\partial t} = \nabla \cdot \left(\frac{r_m^{adh}}{4} \left(3p_{adh} \left(H - \frac{2}{3} \right)^2 + 1 - \frac{4p_{adh}}{3} \right) \nabla H \right) \tag{17}$$

where $H = H_{i,j}(t)$.

D.3 Coarse-graining the Pulling & Adhesion ABM

The Pulling & Adhesion ABM is composed of Rules A to F from Figure 1 and Sections A.1-A.3. We begin coarse-graining this ABM into a PDE model by writing the master system of equations governing how both

$P_{i,j}(t)$ and $H_{i,j}(t)$ change according to these rules:

$$\frac{\partial P_{i,j}(t)}{\partial t} = K^{Rule\ A} + K^{Rule\ B.1} + K^{Rule\ B.2} + K_P^{Rule\ E.1} + K^{Rule\ E.2} \quad (18)$$

$$\frac{\partial H_{i,j}(t)}{\partial t} = K^{Rule\ C} + K^{Rule\ D} + K_H^{Rule\ E.1} + K^{Rule\ F}, \quad (19)$$

where $K_P^{Rule\ E.1}$ denotes how $P_{i,j}(t)$ is affected by Rule E.1 and $K_H^{Rule\ E.1}$ denotes how $H_{i,j}(t)$ is affected by Rule E.1. All other rules affect either $P_{i,j}(t)$ or $H_{i,j}(t)$, but not both. Rules A-D are described in Sections D.1 and D.2, and we do not restate them here.

Rule E specifies how a pulling agent migrates into an empty neighboring lattice site when a neighboring adhesive agent is present in the lattice site opposite the direction of migration. In Rule E.1, the pulling agent successfully pulls the adhesive agent as it migrates, which occurs with probability p_{pull} . In this scenario, the pulling agent shifts into the previously-empty lattice site and the adhesive agent moves into the site previously occupied by the pulling agent. We write this rule in the master equation for $P_{i,j}(t)$ as:

$$\begin{aligned} K_P^{Rule\ E.1} = & -\frac{p_{pull}r_m^{pull}}{4} \left[H_{i,j-1}(t)P_{i,j}(t)0_{i,j+1}(t) + 0_{i,j-1}(t)P_{i,j}(t)H_{i,j+1}(t) + \right. \\ & \left. H_{i-1,j}(t)P_{i,j}(t)0_{i+1,j}(t) + 0_{i-1,j}(t)P_{i,j}(t)H_{i+1,j}(t) \right] \\ & + \frac{p_{pull}r_m^{pull}}{4} \left[H_{i,j-2}(t)P_{i,j-1}(t)0_{i,j}(t) + 0_{i,j}(t)P_{i,j+1}(t)H_{i,j+2}(t) + \right. \\ & \left. H_{i-2,j}(t)P_{i-1,j}(t)0_{i,j}(t) + 0_{i,j}(t)P_{i+1,j}(t)H_{i+2,j}(t) \right], \end{aligned} \quad (20)$$

and in the master equation for $H_{i,j}(t)$ as:

$$\begin{aligned} K_H^{Rule\ E.1} = & -\frac{p_{pull}r_m^{pull}}{4} \left[0_{i,j-2}(t)P_{i,j-1}(t)H_{i,j}(t) + H_{i,j}(t)P_{i,j+1}(t)0_{i,j+2}(t) + \right. \\ & \left. 0_{i-2,j}(t)P_{i-1,j}(t)H_{i,j}(t) + H_{i,j}(t)P_{i+1,j}(t)0_{i+2,j}(t) \right] \\ & + \frac{p_{pull}r_m^{pull}}{4} \left[H_{i,j-1}(t)P_{i,j}(t)0_{i,j+1}(t) + 0_{i,j-1}(t)P_{i,j}(t)H_{i,j+1}(t) + \right. \\ & \left. H_{i-1,j}(t)P_{i,j}(t)0_{i+1,j}(t) + 0_{i-1,j}(t)P_{i,j}(t)H_{i+1,j}(t) \right]. \end{aligned} \quad (21)$$

The neighboring adhesive agent successfully adheres to the migrating pulling agent and aborts its migration event with probability p_{adh} . Neither $P_{i,j}(t)$ or $H_{i,j}(t)$ changes in this scenario as no agents change their locations in response to the adhesion event. In Rule E.2, the adhesive agent fails to adhere to the pulling agent and the pulling agent fails to pull the adhesive agent, which occurs with probability $1 - p_{adh} - p_{pull}$. In this scenario, the pulling agent shifts into the previously-empty lattice site while the neighboring adhesive

agent remains in its previous lattice site. We write this rule in the master equation as:

$$\begin{aligned}
K^{Rule\ E.2} = & -\frac{(1-p_{adh}-p_{pull})r_m^{pull}}{4} \left[H_{i,j-1}(t)P_{i,j}(t)0_{i,j+1}(t) + 0_{i,j-1}(t)P_{i,j}(t)H_{i,j+1}(t) + \right. \\
& \left. H_{i-1,j}(t)P_{i,j}(t)0_{i+1,j}(t) + 0_{i-1,j}(t)P_{i,j}(t)H_{i+1,j}(t) \right] \\
& + \frac{(1-p_{adh}-p_{pull})r_m^{pull}}{4} \left[H_{i,j-2}(t)P_{i,j-1}(t)0_{i,j}(t) + 0_{i,j}(t)P_{i,j+1}(t)H_{i,j+2}(t) + \right. \\
& \left. H_{i-2,j}(t)P_{i-1,j}(t)0_{i,j}(t) + 0_{i,j}(t)P_{i+1,j}(t)H_{i+2,j}(t) \right]. \quad (22)
\end{aligned}$$

Rule F specifies how adhesive agents migrate into an empty neighboring lattice site when a neighboring pulling agent is in the lattice site opposite the direction of migration. The two agents do not interact with each other in this scenario. As such, the adhesive agent migrates into the empty lattice site with rate $r_m^{adh}/4$. We write this rule in the master equation as:

$$\begin{aligned}
K^{Rule\ F} = & -\frac{r_m^{adh}}{4} \left[P_{i,j-1}(t)H_{i,j}(t)0_{i,j+1}(t) + 0_{i,j-1}(t)H_{i,j}(t)P_{i,j+1}(t) + \right. \\
& \left. P_{i-1,j}(t)H_{i,j}(t)0_{i+1,j}(t) + 0_{i-1,j}(t)H_{i,j}(t)P_{i+1,j}(t) \right] \\
& + \frac{r_m^{adh}}{4} \left[P_{i,j-2}(t)H_{i,j-1}(t)0_{i,j}(t) + 0_{i,j}(t)H_{i,j+1}(t)P_{i,j+2}(t) + \right. \\
& \left. P_{i-2,j}(t)H_{i-1,j}(t)0_{i,j}(t) + 0_{i,j}(t)H_{i+1,j}(t)P_{i+2,j}(t) \right]. \quad (23)
\end{aligned}$$

To obtain the resulting system of differential equations for the Pulling & Adhesion ABM, we substitute Equations (8), (9), (10), (14), (15), (20), (21), (22), and (23) into Equation (19) and set $0_{i,j} = 1 - T_{i,j}$, where $T_{i,j} = P_{i,j} + H_{i,j}$. We replace each term with its Taylor expansion, up to second order, from Equations (11) and (16). As shown in the Mathematica notebook **Pulling-Adhesion_coarse_graining.nb**, taking the limit of the resulting expression as $\Delta \rightarrow 0$ leads to the mean-field system of PDEs for the Pulling & Adhesion ABM:

$$\begin{aligned}
\frac{\partial P}{\partial t} = & \frac{r_m^{pull}}{4} \nabla \cdot \left((1-T)\nabla P + P\nabla T \right) \\
& + p_{adh} \frac{r_m^{pull}}{4} \nabla \cdot \left(-3P(1-T)\nabla H - H(1-T)\nabla P - HP\nabla T \right) \\
& + p_{pull} \frac{r_m^{pull}}{4} \nabla \cdot \left(3P^2\nabla T \right) \\
\frac{\partial H}{\partial t} = & \frac{r_m^{adh}}{4} \nabla \cdot \left((1-T)\nabla H + H\nabla T \right) \\
& + p_{adh} \frac{r_m^{adh}}{4} \nabla \cdot \left(-4(1-T)H\nabla H - H^2\nabla T \right) \\
& + p_{pull} \frac{r_m^{pull}}{4} \nabla \cdot \left(-(1-T)H\nabla P + (1-T)P\nabla H + 3HP\nabla T \right), \quad (24)
\end{aligned}$$

where $P = P_{i,j}(t)$, $H = H_{i,j}(t)$, and $T = T_{i,j}(t)$.

E BINN implementation and training

E.1 BINNs architecture

Following [30], we construct $T^{MLP}(x, t)$ using a fully-connected feed-forward MLP with three hidden layers, which can be written as:

$$\begin{aligned}
 z_0 &= [x, t] \\
 z_1 &= \sigma(z_0 W_1 + b_1) \\
 z_2 &= \sigma(z_1 W_2 + b_2) \\
 z_3 &= \sigma(z_2 W_3 + b_3) \\
 T^{MLP}(x, t) &= \psi(z_3 W_4 + b_4),
 \end{aligned} \tag{25}$$

where each z_k denotes the k^{th} hidden layer for $k = 1, 2, 3$; the W_k matrices and the b_k vectors provide the weights and biases of each hidden layer, respectively; σ denotes the sigmoid activation function $\sigma(x) = 1/(1 + \exp(-x))$, and ψ denotes the softplus activation function $\psi(x) = \log(1 + \exp(x))$. Each hidden layer in Equation (25) has 128 neurons, meaning that $W_1 \in \mathbb{R}^{2 \times 128}$; $W_2, W_3 \in \mathbb{R}^{128 \times 128}$; $W_4 \in \mathbb{R}^{128 \times 1}$; $b_1, b_2, b_3 \in \mathbb{R}^{128}$; and $b_4 \in \mathbb{R}$.

The architecture of $\mathcal{D}^{MLP}(T)$ is identical to the architecture for T^{MLP} in Equation (25), except \mathcal{D}^{MLP} has a one-dimensional input vector, T , instead of the two-dimensional input vector, $[x, t]$.

E.2 Loss Function

BINNs are trained to concurrently fit the given dataset, $\langle T^{ABM}(x, t) \rangle^{train}$, and solve Equation (5) by minimizing the following multi-term loss function:

$$\mathcal{L}_{total} = \mathcal{L}_{WLS} + \epsilon \mathcal{L}_{PDE} + \mathcal{L}_{constr}. \tag{26}$$

The ϵ parameter ensures the terms \mathcal{L}_{WLS} and \mathcal{L}_{PDE} are equally weighted because these terms can be of different orders of magnitude; we find good results for $\epsilon = 10^4$.

The \mathcal{L}_{WLS} term of Equation (26) computes a weighted mean-squared error between $T^{MLP}(x, t)$ and $\langle T^{ABM}(x, t) \rangle^{train}$:

$$\mathcal{L}_{WLS} = \frac{1}{T_f^{train} X} \sum_{i=1, j=1}^{X, T_f^{train}} w_{i,j} \left(T^{MLP}(x_i, t_j) - \langle T^{ABM}(x_i, t_j) \rangle \right)^2. \tag{27}$$

We set $w_{i,1} = 10.0$ for all values of i and all other $w_{i,j}$ values to 1.0 to ensure that T^{MLP} closely agrees with the ABM's initial data. By minimizing Equation (27), we ensure $T^{MLP}(x, t)$ closely approximates $\langle T^{ABM}(x, t) \rangle^{train}$.

The \mathcal{L}_{PDE} term of Equation (26) quantifies how closely T^{MLP} and \mathcal{D}^{MLP} follow Equation (5). To ensure the MLPs satisfy this PDE framework throughout the ABM's entire spatiotemporal domain, we

uniformly sample 10,000 points, $\{(x_k, t_k)\}_{k=1}^{10,000}$, from $[0, X] \times [0, 750]$. For notational convenience, let $\hat{T}_k = T^{MLP}(x_k, t_k)$ and $\hat{D}_k = \mathcal{D}^{MLP}(T^{MLP}(x_k, t_k))$. We then compute the mean-squared error between the left- and right-hand sides of Equation (5) at all sampled points:

$$\mathcal{L}_{PDE} = \frac{1}{10,000} \sum_{i=1}^{10,000} \left[\frac{\partial}{\partial t} \hat{T}_k - \frac{\partial}{\partial x} \left(\hat{D}_k \frac{\partial \hat{T}_k}{\partial x} \right) \right]^2, \quad (28)$$

where differentiation of T^{MLP} and \mathcal{D}^{MLP} is performed using automatic differentiation. Minimizing Equation (28) verifies that T^{MLP} and \mathcal{D}^{MLP} together satisfy Equation (5).

The \mathcal{L}_{constr} term of Equation (26) incorporates user knowledge into BINNs training. We penalize \mathcal{D}^{MLP} for outputting values outside of the interval $[D_{\min}, D_{\max}]$. We set $D_{\min} = 0$ because Equation (5) is ill-posed if $\mathcal{D}(u) < 0$, and we set $D_{\max} = 1.0$ because the mean-field rates of diffusion are below one for all ABM simulations in this study. We compute this term by squaring any values of \hat{D}_i that are not within $[D_{\min}, D_{\max}]$ and weighting these values by 10^{10} :

$$\mathcal{L}_{constr} = \frac{1}{10,000} \sum_{\substack{k=1 \\ \hat{D}_k \notin [D_{\min}, D_{\max}]}}^{10,000} 10^{10} (\hat{D}_k)^2. \quad (29)$$

This term regularizes the BINN training procedure to prevent \mathcal{D}^{MLP} from outputting unrealistic values.

E.3 BINN Training Procedure

For BINN model training, we randomly partition the training ABM dataset into 80%/20% BINN training and BINN validation datasets. We train the BINN parameter values (i.e., the weights and biases for T^{MLP} and \mathcal{D}^{MLP}) to minimize a loss function, \mathcal{L} , using the gradient-based ADAM optimizer with its default hyperparameter values on the BINN training dataset. For each new set of BINN parameters, we compute \mathcal{L} on the BINN validation dataset and save the BINN parameters if the newly computed \mathcal{L} value achieves a 1% or greater relative improvement over the previous smallest recorded value. Following [38], we perform training in a two-step process: in the first step, we train the BINN to match the ABM data by optimizing $\mathcal{L} = \mathcal{L}_{WLS}$ from Equation (27); in the second step, we train the BINN on $\mathcal{L} = \mathcal{L}_{total}$ from Equation (26). The first training step is performed for 10^4 epochs with an early stopping criterion of 10^3 , meaning that training ends early if the smallest-computed \mathcal{L} value on the validation data is unchanged for 10^3 epochs. The second step is performed for 10^6 epochs with an early stopping criterion of 10^5 . Each epoch is computed in minibatches of size 10^3 . BINN model training is performed using the PyTorch deep learning library (version 1.7.1).

Following [30], we train five separate BINNs for each ABM dataset using different BINN training and validation datasets because the final trained model can be sensitive to which data is included in these two datasets. We compute the five PDE forward simulations from these trained models and select whichever BINN achieves the smallest mean-squared error against the ABM training data as the final selected BINN model.

F Numerical integration of PDEs

When simulating Equation (6), we populate the middle 20% of the spatial dimension with 75% confluence and zero confluence everywhere else to match the initial ABM configurations and implement no-flux boundary conditions:

$$T(x, 0) = \begin{cases} 0.75, & 80 \leq x \leq 120 \\ 0, & \text{otherwise,} \end{cases},$$

$$\frac{\partial T}{\partial x}(0, t) = \frac{\partial T}{\partial x}(X, t) = 0. \quad (30)$$

Before integration, we discretize the spatial domain as $x_i = i\Delta x$ with $i = 0, \dots, 199$ and $\Delta x = 1.0$. For ease of notation, let $T_i(t) = T(x_i, t)$ and $\mathcal{D}_i(t) = \mathcal{D}(T_i(t))$. We then use the method of lines approach to integrate Equation (6). To discretize the right hand side of Equation (6), we let

$$\frac{\partial T_i(t)}{\partial x} \left(\mathcal{D}_i(t) \frac{\partial T_i(t)}{\partial x} \right) \approx \frac{P_{i+1/2}(t) - P_{i-1/2}(t)}{\Delta x},$$

where $P_{i\pm 1/2}(t)$ denotes the right or left flux through location x_i , respectively. Following [52], we approximate these fluxes by

$$P_{i+1/2}(t) = \frac{1}{2} \left(\mathcal{D}_i(t) \frac{T_{i+1}(t) - T_i(t)}{\Delta x} + \mathcal{D}_{i+1}(t) \frac{T_{i+1}(t) - T_i(t)}{\Delta x} \right)$$

$$P_{i-1/2}(t) = \frac{1}{2} \left(\mathcal{D}_{i-1}(t) \frac{T_i(t) - T_{i-1}(t)}{\Delta x} + \mathcal{D}_i(t) \frac{T_i(t) - T_{i-1}(t)}{\Delta x} \right). \quad (31)$$

To implement the no-flux boundary conditions, we incorporate the ghost points x_{-1} and x_{200} that enforce $u_{-1}(t) = u_1(t)$ and $u_{198}(t) = u_{200}(t)$ into Equation (31). We integrate Equation (6) using the `odeint` command from Scipy's integration package (version 1.8.0), which implements the Livermore Solver for Differential Equations (LSODA) method [53].

G Supplementary figures

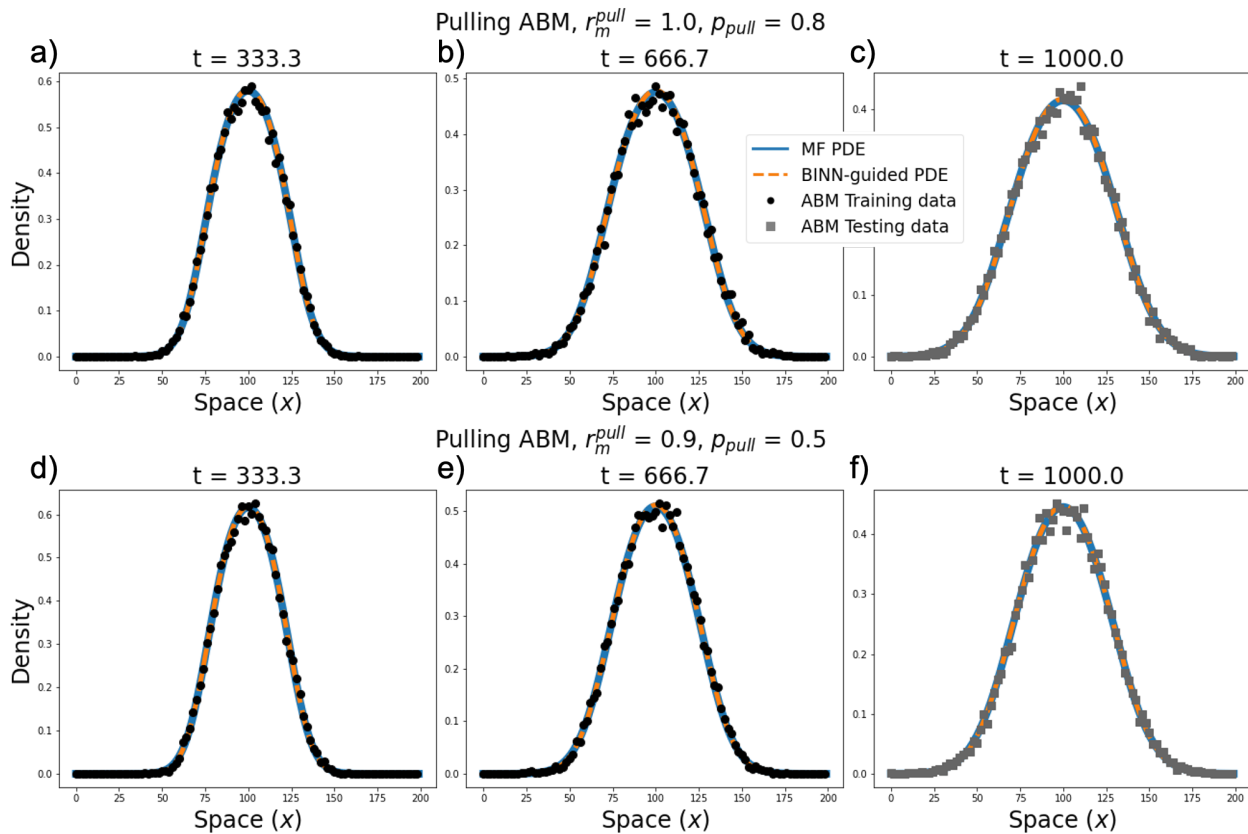


Figure 12: Forecasting Pulling ABM data with mean-field (MF) and BINN-guided PDE models. The mean-field and BINN-guided PDE simulations are used to forecast Pulling ABM data for (a-c) $r_m^{pull} = 1.0, p_{pull} = 0.8$ (d-f) $r_m^{pull} = 0.9, p_{pull} = 0.5$.

Sample	$\boldsymbol{p} = (r_m^{adh}, p_{adh})^T$
1	$(0.145, 0.825)^T$
2	$(0.505, 0.575)^T$
3	$(0.415, 0.725)^T$
4	$(0.865, 0.525)^T$
5	$(0.955, 0.625)^T$
6	$(0.235, 0.775)^T$
7	$(0.685, 0.675)^T$
8	$(0.325, 0.875)^T$
9	$(0.775, 0.925)^T$
10	$(0.595, 0.975)^T$

Table 5: Latin hypercube sampling for the Adhesion ABM. The samples from the new parameter dataset for the Adhesion ABM when varying r_m^{adh} and p_{adh} . The samples are ordered by increasing testing MSE values (see Figure 10(c)).

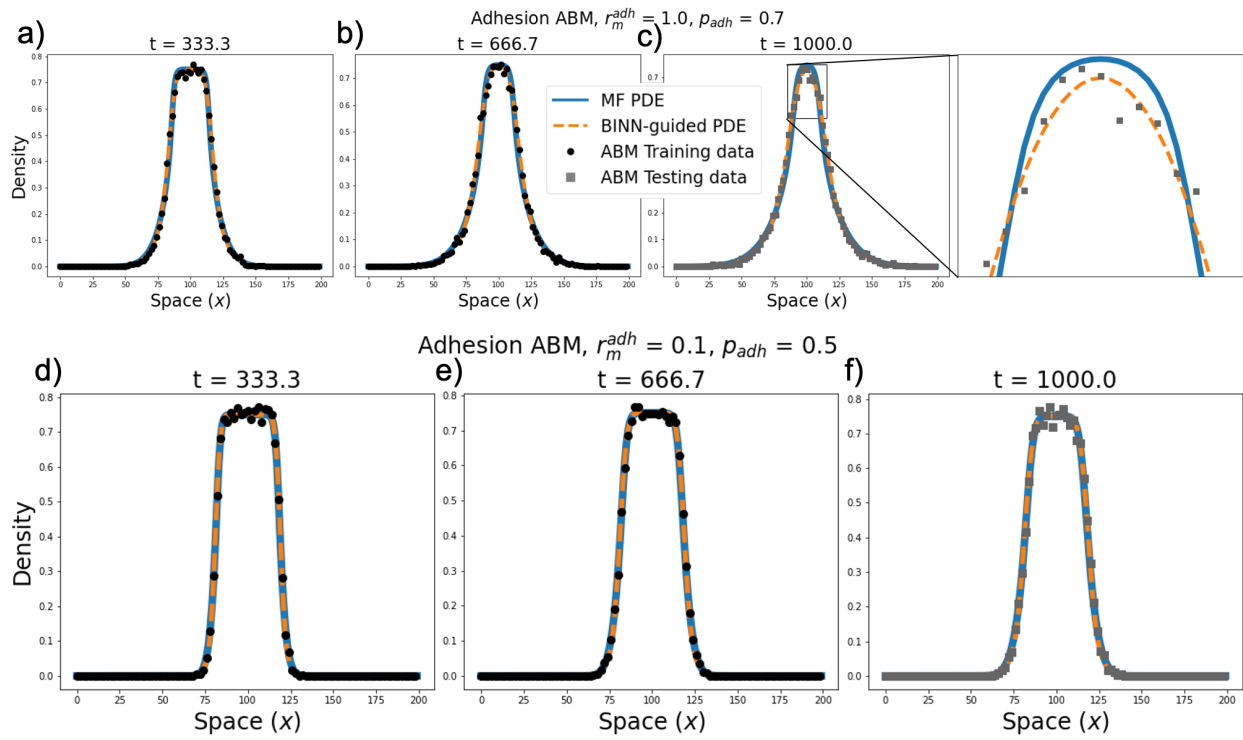


Figure 13: Forecasting Adhesion ABM data with mean-field and BINN-guided PDE models. The mean-field and BINN-guided PDE simulations are used to forecast Adhesion ABM data for (a-c) $r_m^{adh} = 1.0, p_{adh} = 0.7$ (d-f) $r_m^{adh} = 0.1, p_{adh} = 0.5$.

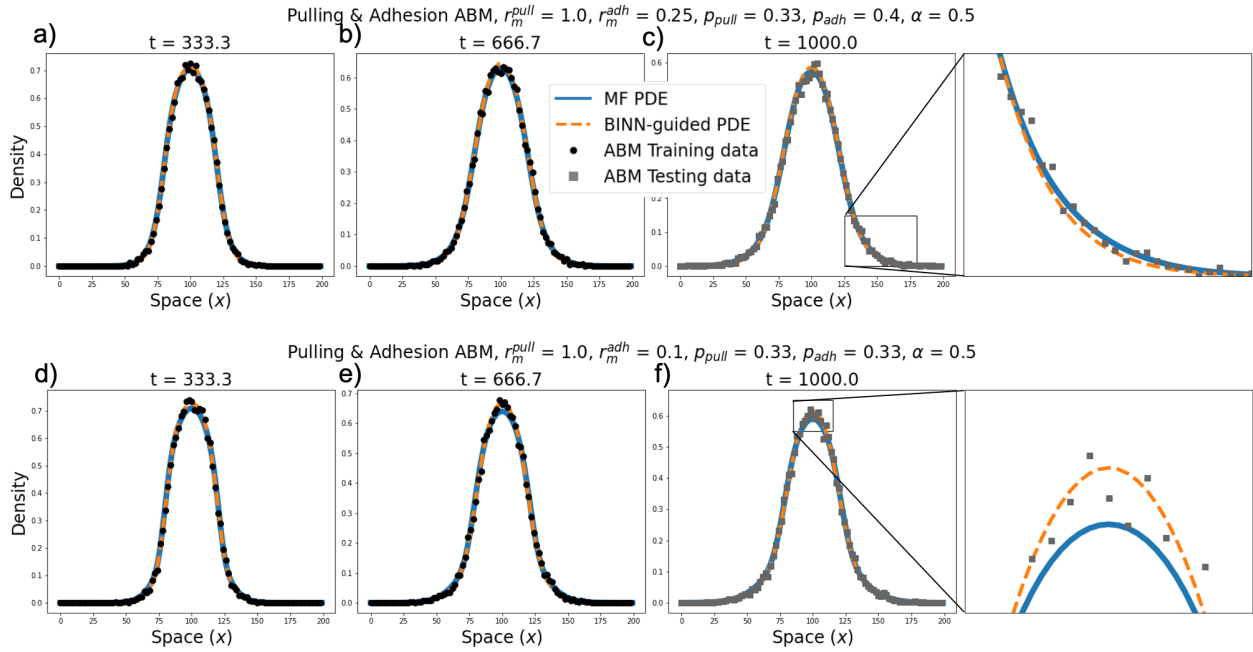


Figure 14: Forecasting Pulling & Adhesion ABM data with mean-field (MF) and BINN-guided PDE models. The mean-field and BINN-guided PDE simulations are used to forecast Pulling & Adhesion ABM data for the base parameter values ($r_m^{pull} = 1.0, r_m^{adh} = 0.25, p_{pull} = 0.33, p_{adh} = 0.33$, and $\alpha = 0.5$), except (a-c) $p_{adh} = 0.4$ (d-f) $r_m^{adh} = 0.1$.

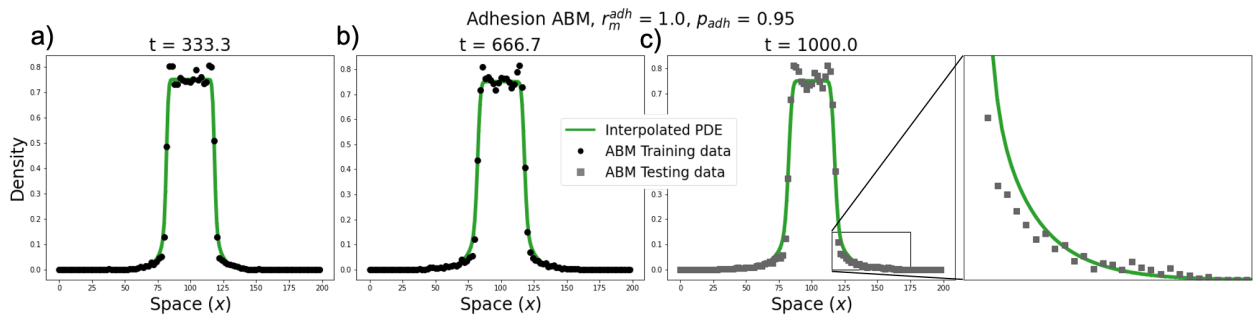


Figure 15: Predicting Adhesion ABM data with the interpolated PDE model. The interpolated PDE model predicts Adhesion ABM data for (a-c) $r_m^{adh} = 1.0$ and $p_{adh} = 0.95$.

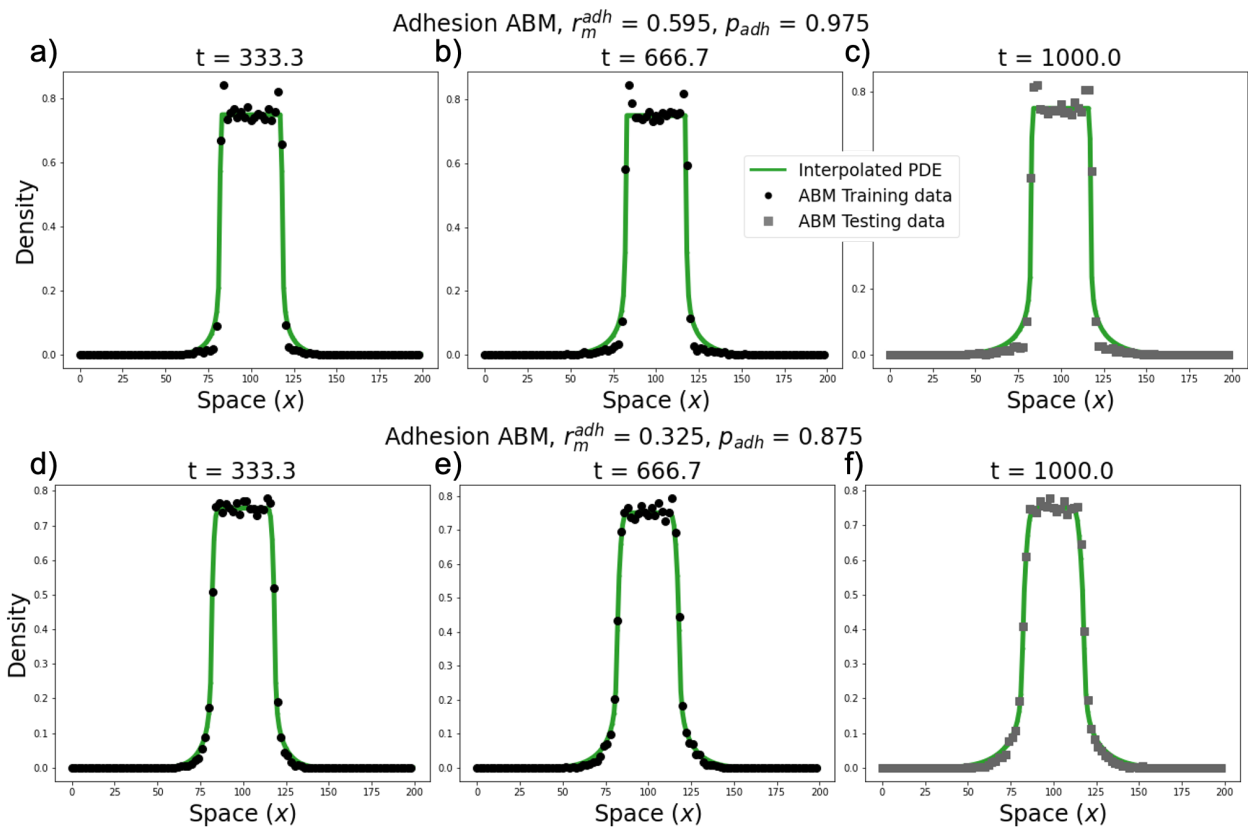


Figure 16: Predicting Adhesion ABM data with the interpolated PDE model. The interpolated PDE model predicts Adhesion ABM data for (a-c) $r_m^{adh} = 0.595$ and $p_{adh} = 0.975$ and (d-f) $r_m^{adh} = 0.325$ and $p_{adh} = 0.875$.

Sample	$\mathbf{p} = (r_m^{pull}, r_m^{adh}, p_{pull}, p_{adh}, \alpha)^T$
1	(1.0, 0.25, 0.394, 0.578, 0.912) ^T
2	(1.0, 0.25, 0.293, 0.528, 0.938) ^T
3	(1.0, 0.25, 0.008, 0.226, 0.988) ^T
4	(1.0, 0.25, 0.511, 0.477, 0.862) ^T
5	(1.0, 0.25, 0.41, 0.109, 0.962) ^T
6	(1.0, 0.25, 0.075, 0.595, 0.888) ^T
7	(1.0, 0.25, 0.042, 0.544, 0.838) ^T
8	(1.0, 0.25, 0.327, 0.059, 0.712) ^T
9	(1.0, 0.25, 0.444, 0.31, 0.662) ^T
10	(1.0, 0.25, 0.209, 0.209, 0.612) ^T
11	(1.0, 0.25, 0.126, 0.41, 0.762) ^T
12	(1.0, 0.25, 0.193, 0.042, 0.588) ^T
13	(1.0, 0.25, 0.059, 0.561, 0.462) ^T
14	(1.0, 0.25, 0.243, 0.26, 0.788) ^T
15	(1.0, 0.25, 0.427, 0.494, 0.512) ^T
16	(1.0, 0.25, 0.595, 0.327, 0.812) ^T
17	(1.0, 0.25, 0.025, 0.461, 0.388) ^T
18	(1.0, 0.25, 0.377, 0.176, 0.488) ^T
19	(1.0, 0.25, 0.226, 0.645, 0.538) ^T
20	(1.0, 0.25, 0.528, 0.126, 0.688) ^T
21	(1.0, 0.25, 0.561, 0.075, 0.562) ^T
22	(1.0, 0.25, 0.142, 0.193, 0.362) ^T
23	(1.0, 0.25, 0.31, 0.092, 0.738) ^T
24	(1.0, 0.25, 0.176, 0.662, 0.412) ^T
25	(1.0, 0.25, 0.645, 0.008, 0.638) ^T
26	(1.0, 0.25, 0.343, 0.293, 0.312) ^T
27	(1.0, 0.25, 0.092, 0.611, 0.238) ^T
28	(1.0, 0.25, 0.109, 0.628, 0.012) ^T
29	(1.0, 0.25, 0.159, 0.343, 0.212) ^T
30	(1.0, 0.25, 0.26, 0.142, 0.188) ^T
31	(1.0, 0.25, 0.36, 0.377, 0.262) ^T
32	(1.0, 0.25, 0.276, 0.36, 0.038) ^T
33	(1.0, 0.25, 0.578, 0.243, 0.288) ^T
34	(1.0, 0.25, 0.628, 0.159, 0.062) ^T
35	(1.0, 0.25, 0.477, 0.511, 0.138) ^T
36	(1.0, 0.25, 0.611, 0.276, 0.338) ^T
37	(1.0, 0.25, 0.461, 0.444, 0.162) ^T
38	(1.0, 0.25, 0.544, 0.427, 0.112) ^T
39	(1.0, 0.25, 0.494, 0.394, 0.088) ^T
40	(1.0, 0.25, 0.662, 0.025, 0.438) ^T

Table 6: Latin hypercube sampling for the Pulling & Adhesion ABM. The samples from the prior parameter dataset for the Pulling & Adhesion ABM when varying p_{pull} , p_{adh} , and α . The samples are ordered by increasing training MSE values.

Sample	$\mathbf{p} = (r_m^{pull}, r_m^{adh}, p_{pull}, p_{adh}, \alpha)^T$
1	$(1.0, 0.25, 0.285, 0.519, 0.775)^T$
2	$(1.0, 0.25, 0.419, 0.352, 0.875)^T$
3	$(1.0, 0.25, 0.486, 0.117, 0.525)^T$
4	$(1.0, 0.25, 0.553, 0.285, 0.375)^T$
5	$(1.0, 0.25, 0.385, 0.586, 0.475)^T$
6	$(1.0, 0.25, 0.586, 0.184, 0.175)^T$
7	$(1.0, 0.25, 0.62, 0.151, 0.325)^T$
8	$(1.0, 0.25, 0.184, 0.084, 0.625)^T$
9	$(1.0, 0.25, 0.352, 0.385, 0.925)^T$
10	$(1.0, 0.25, 0.653, 0.05, 0.275)^T$
11	$(1.0, 0.25, 0.151, 0.653, 0.075)^T$
12	$(1.0, 0.25, 0.452, 0.251, 0.125)^T$
13	$(1.0, 0.25, 0.084, 0.218, 0.225)^T$
14	$(1.0, 0.25, 0.318, 0.62, 0.725)^T$
15	$(1.0, 0.25, 0.519, 0.017, 0.825)^T$
16	$(1.0, 0.25, 0.117, 0.419, 0.425)^T$
17	$(1.0, 0.25, 0.251, 0.486, 0.975)^T$
18	$(1.0, 0.25, 0.017, 0.452, 0.025)^T$
19	$(1.0, 0.25, 0.05, 0.318, 0.575)^T$
20	$(1.0, 0.25, 0.218, 0.553, 0.675)^T$

Table 7: Latin hypercube sampling for the Pulling & Adhesion ABM. The samples from the new parameter dataset for the Pulling & Adhesion ABM when varying p_{pull} , p_{adh} , and α . The samples are ordered by increasing training MSE values.

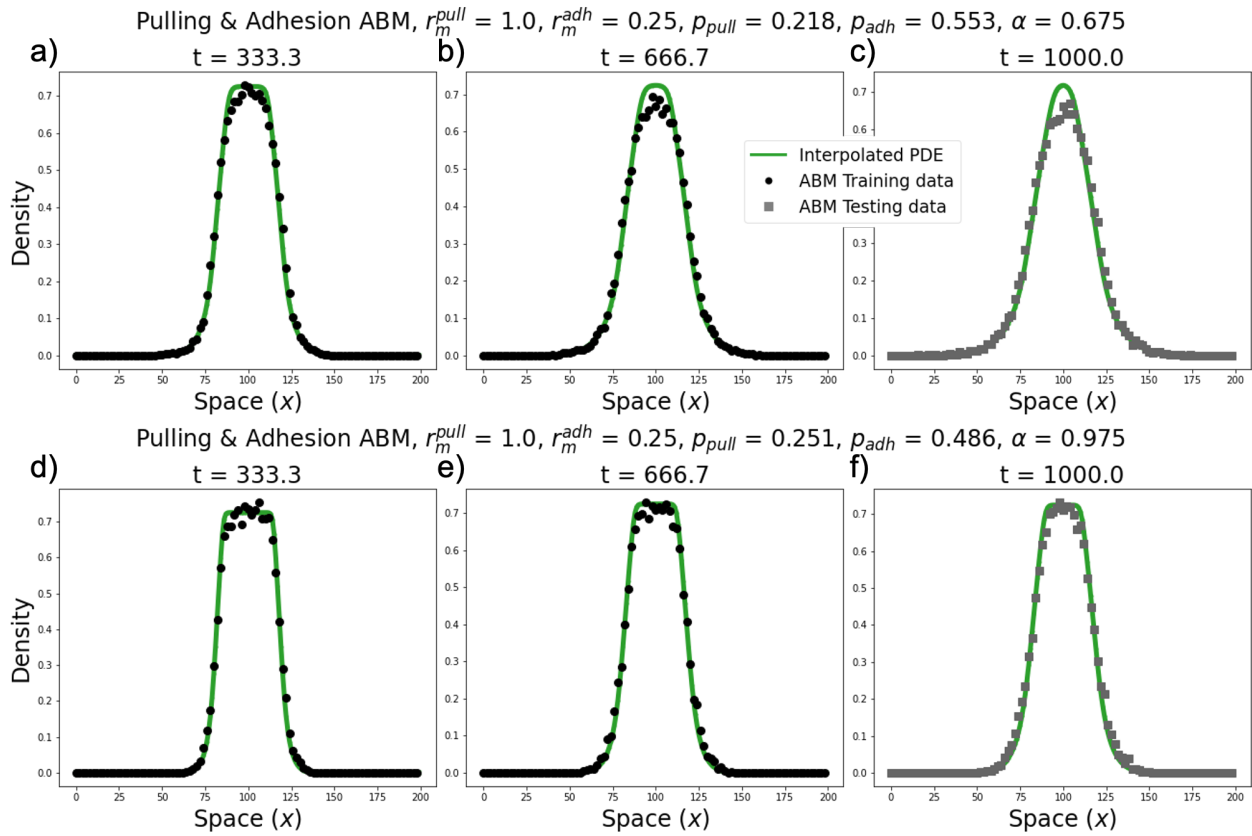


Figure 17: Predicting Pulling & Adhesion ABM data with the interpolated PDE model. The interpolated PDE model predicts Adhesion ABM data for $r_m^{pull} = 1.0$, $r_m^{adh} = 0.25$, and (a-c) $p_{pull} = 0.218$, $p_{adh} = 0.553$, and $\alpha = 0.675$ (d-f) $p_{pull} = 0.251$, $p_{adh} = 0.486$, and $\alpha = 0.975$.

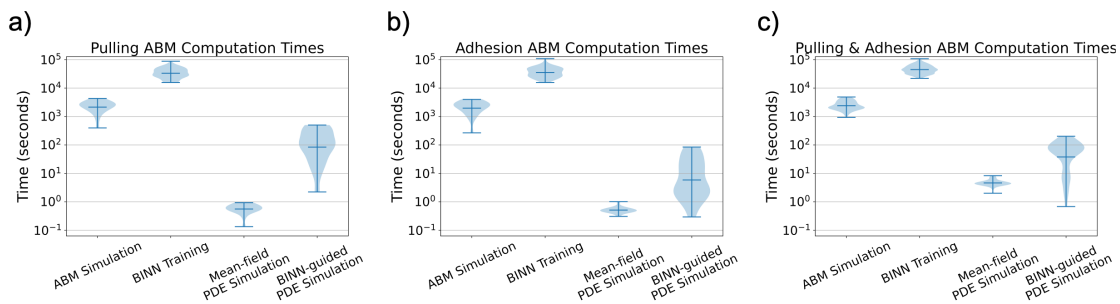


Figure 18: Computational expenses of each modeling approach. Violin plots represent the distribution of wall time computations for ABM simulations, BINN training, mean-field PDE simulations, and BINN-guided PDE simulations for the (a) Pulling ABM, (b) Adhesion ABM, and (c) Pulling & Adhesion ABM.